



DISEASES AND DISORDERS

A dynamic in vitro model of Down syndrome neurogenesis with trisomy 21 gene dosage correction

Prakhar Bansal^{1,2,†}, Erin C. Banda^{2,†}, Heather R. Glatt-Deeley², Christopher E. Stoddard³, Jeremy W. Linsley^{4,5}, Neha Arora^{4,‡}, Cécile Deleschaux^{2,§}, Darcy T. Ahern^{1,2,¶}, Yuvabharath Kondaveeti^{2,‡}, Rachael E. Massey^{1,2,6}, Michael Nicouleau^{2,*,¶}, Shijie Wang⁴, Miguel Sabariego-Navarro⁷, Mara Dierssen^{7,8,9,10}, Steven Finkbeiner^{4,5,11,12}, Stefan F. Pinter^{1,2,6,*}

Excess gene dosage from chromosome 21 (chr21) causes Down syndrome (DS), spanning developmental and acute phenotypes in terminal cell types. Which phenotypes remain amenable to intervention after development is unknown. To address this question in a model of DS neurogenesis, we derived trisomy 21 (T21) human induced pluripotent stem cells (iPSCs) alongside, otherwise, isogenic euploid controls from mosaic DS fibroblasts and equipped one chr21 copy with an inducible *XIST* transgene. Monoallelic chr21 silencing by *XIST* is near-complete and irreversible in iPSCs. Differential expression reveals that T21 neural lineages and iPSCs share suppressed translation and mitochondrial pathways and activate cellular stress responses. When *XIST* is induced before the neural progenitor stage, T21 dosage correction suppresses a pronounced skew toward astrogenesis in neural differentiation. Because our transgene remains inducible in postmitotic T21 neurons and astrocytes, we demonstrate that *XIST* efficiently represses genes even after terminal differentiation, which will empower exploration of cell type-specific T21 phenotypes that remain responsive to chr21 dosage.

INTRODUCTION

As the most prevalent viable human aneuploidy [trisomy 21 (T21) in up to 1:800 to 1:1000 live births], Down syndrome (DS) poses three substantial challenges to understanding and addressing the clinical needs of people living with DS (1). First, our understanding of the developmental etiology underlying cardiac, hematopoietic, and neurological defects in DS is still limited (2). Ever-more sophisticated rodent DS models faithfully carry most of human chromosome 21 (chr21) (3, 4) or traverse syntenic boundaries to represent supernumerary mouse orthologs of chr21 genes (5). While these rodent models capture many important aspects of DS, human T21 induced pluripotent stem cells (iPSCs) are serving as an important complementary model for DS development and preclinical research (6). These iPSC models may prove especially relevant to human-specific aspects of development, for example, by reflecting brain region-specific neural cell types (7), intrinsically longer human neuronal

maturation (8), and a more rapidly evolving susceptibility to neurodegeneration that may be rooted in human neurodevelopment (9, 10).

Second, we lack experimental approaches to systematically distinguish irreversible developmental phenotypes from “acute” cellular phenotypes that may remain amenable to postnatal intervention. Supernumerary chr21 genes, or their rodent orthologs, are present throughout differentiation or development of these DS iPSC and rodent DS models, respectively. With few exceptions (11), we therefore have an incomplete view of which T21 phenotypes depend on ongoing excess dosage of specific chr21 genes in terminally differentiated cells. This question is particularly relevant to DS-associated neurodegeneration (12).

Third, cellular stress pathways that are chronically and systemically active in DS (13–18) and likely play an important role in DS neurodegeneration (19) are also shared with human trisomies T13 and T18 (20). In contrast, transcriptional changes observed in dosage-compensated trisomy-X are limited in assessed cell types (21, 22), and, congruently, >90% of individuals with trisomy-X are diagnosed either late in life or never on account of comparatively mild phenotypes (23). The most plausible origin for aneuploidy-associated cellular stress common to T13, T18, and T21 is the cumulative excess expression of the many autosomal genes that code for subunits of dosage-sensitive protein complexes. However, this interpretation has not yet been tested formally in the context of an autosomal trisomy, as it requires distinguishing excess expression from the mere presence of the supernumerary chromosome.

A human cellular model with dynamic T21 gene dosage would be instrumental toward addressing these challenges, across a range of DS-affected cell fates and phenotypes. To characterize the impact of T21 in iPSCs and terminally differentiated cell types, we generated our own dynamic human iPSC model of T21 dosage, alongside otherwise isogenic controls from mosaic DS. Pioneering work by Lawrence and colleagues (24) demonstrated the utility of the long noncoding RNA *XIST*, which endogenously silences the inactive

¹Graduate Program in Genetics and Developmental Biology, UCONN Health, University of Connecticut, Farmington, CT, USA. ²Department of Genetics and Genome Sciences, UCONN Health, University of Connecticut, Farmington, CT, USA. ³Cell and Genome Engineering Core, UCONN Health, University of Connecticut, Farmington, CT, USA. ⁴Center for Systems and Therapeutics, Gladstone Institutes, San Francisco, CA, USA. ⁵Taube/Koret Center for Neurodegenerative Disease, Gladstone Institutes, San Francisco, CA, USA. ⁶Institute for Systems Genomics, University of Connecticut, Farmington, CT, USA. ⁷Centre for Genomic Regulation (CRG), The Barcelona Institute of Science and Technology, Barcelona, Spain. ⁸Universitat Pompeu Fabra (UPF), Barcelona, Spain. ⁹Human Pharmacology and Clinical Neurosciences Research Group, Neurosciences Research Program, Hospital Del Mar Medical Research Institute (IMIM), Barcelona, Spain. ¹⁰Centro de Investigación Biomédica en Red de Enfermedades Raras (CIBERER), Madrid, Spain. ¹¹Departments of Neurology and Physiology, University of California San Francisco, San Francisco, CA, USA. ¹²Neuroscience and Biomedical Sciences Graduate Programs, University of California San Francisco, San Francisco, CA, USA.

*Corresponding author. Email: spinter@uchc.edu

†These authors contributed equally to this work.

‡Present address: Department of Biology, Brandeis University, Waltham, MA, USA.

§Present address: UMR_S1134, Université Paris Cité, Paris, France.

¶Present address: Intellia Therapeutics, Cambridge, MA, USA.

#Present address: Enzerna Biosciences, Morrisville, NC, USA.

**Present address: Early Drug Discovery Unit, Montreal Neurology Institute, McGill University, Montréal, Québec, Canada.

X in females, for T21 dosage correction in DS iPSCs. *XIST* RNA spreads from its site of transcription across the entire chromosome in cis to directly and indirectly recruit orthogonal repressive chromatin complexes to silence genes (25). However, earlier work in the mouse system indicated that *Xist* could establish gene silencing only during or upon exiting pluripotency, but not after differentiation (26, 27), with rare exception (28, 29). Recent work by the Lawrence laboratory (30) shows that human *XIST* can still silence genes up to the neural progenitor cell (NPC) stage, but technical limitations hindered *XIST* induction in terminal, postmitotic human neural cells.

Here, we leverage phased allelic expression analysis to demonstrate that our new inducible T21-*XIST* design enables uniform, near-complete and irreversible T21 dosage correction in iPSCs. *XIST* suppresses T21 trans-effects, including cellular stress pathways that are also active in T21 neural lineages. T21 silencing before the NPC stage rescues T21-altered neuroastroglial lineage balance that reflects excess gliogenesis previously observed in DS fetal samples (31–35) and rodent models (36–38). Because our T21-*XIST* system also effectively induces *XIST* and represses chr21 dosage in postmitotic neurons and astrocytes, this new model of dynamic T21 gene dosage will facilitate identification of cellular pathways and cell types that may present promising targets for intervention after completed development.

RESULTS

T21 dosage correction by *XIST*-mediated monoallelic silencing in DS iPSCs

To derive T21 iPSCs alongside isogenic euploid control lines, we reprogrammed dermal fibroblasts from a male individual with mosaic DS (39) and screened the resulting iPSC clones using copy number (CN)-sensitive quantitative polymerase chain reaction (qPCR) (fig. S1, A and B). Two T21 lines appeared to have a gain on chr17, a frequent karyotypic abnormality primarily observed in human embryonic stem cells (40, 41), but featured only two centromere 17 signals by fluorescent in situ hybridization (FISH) follow-up (fig. S1C). We performed array comparative genomic hybridization (aCGH; CytoSNP-850k) to confirm expected karyotypes for fibroblasts, euploid and T21 iPSCs, and to resolve segmental (17q) gains in the two corresponding clones, which were excluded thereafter (fig. S1D). Differential probe intensity analysis of the remaining T21 and euploid iPSC lines also revealed a large set of heterozygous single-nucleotide polymorphisms (SNPs) with increased representation in the euploid lines spanning chr21 and a smaller focal set that was lost in euploid lines (fig. S1E). These results suggested that one chr21 copy from each parent is maintained in euploid lines (chr21^M and chr21^P), whereas T21 iPSCs carry an additional copy (chr21^{M2}), likely a maternal chromatid retained via nondisjunction in meiosis II (42).

While T21 is stably maintained in iPSCs after reprogramming (43–45), sporadic T21 loss has been reported (46, 47). We therefore confirmed the mitotic stability of three chr21 copies by two independent approaches. First, three independent signals were observed in 94.5% of T21 iPSCs by FISH (*DSCR8* probe), compared to 99% of euploid iPSCs with two signals (fig. S1F). Second, while targeting a *UBC* promoter-driven doxycycline (dox)-responsive transactivator (rTTA3G) to the Adeno-Associated Virus Integration Site 1 (AAVS1) safe harbor in *PPP1R12C* (chr19), we confirmed that all 32

of 32 independent colonies arising from single cells maintained T21 by CN-sensitive qPCR for a *DYRK1A* amplicon (fig. S1G).

We integrated our third generation tet responsive promoter (TRE3G)-driven *XIST* cDNA transgene on chr21^P (Fig. 1A), after reverifying the karyotypic integrity of rTTA3G clones by aCGH (fig. S1D). To this end, we designed Cas9 guides dependent on a chr21^P-specific protospacer adjacent motif, targeting an intergenic site well outside of *DYRK1A* to avoid impacting its expression. We proceeded with three independent, PCR-screened T21-*XIST* clones and tested for *XIST* induction by RNA-FISH, and immunofluorescence (IF) staining for ubiquitinated histone 2A lysine 119 (H2AK119ub) and trimethylated histone 3 lysine 27 (H3K27me3), which follow *XIST/Xist* RNA expression on mouse and human X alike (25). Notably, because the original fibroblasts were from a male individual with DS (fig. S1C), there was no endogenous *XIST* expression, and any *XIST*/H2AK119ub/H3K27me3 cloud must arise from the T21-targeted *XIST* transgene on chr21. After cessation of acute dox treatment [3 weeks of dox withdrawal (w/d)] iPSCs were negative for *XIST*, underscoring that the TRE3G system is not leaky and turns off when dox is withdrawn, whereas virtually all T21-*XIST* iPSCs displayed *XIST* clouds and acquired H2AK119ub/H3K27me3 signals in the presence of dox (Fig. 1, B and C). Together, these data illustrate the homogeneity of *XIST* induction and provide independent confirmation that this third copy of chr21 is faithfully maintained in iPSCs.

We next performed mRNA sequencing (mRNA-seq) of euploid, T21, and T21-*XIST* iPSCs to confirm high uniformity in pluripotency genes over lineage-specific markers (fig. S2A) and to quantify T21 dosage correction by *XIST* in the presence, absence, or upon withdrawal of dox (Fig. 1, B to D), which tests whether gene silencing is maintained once established. *XIST* was uniformly expressed in all three T21-*XIST* clones at 3, 6, and 9 weeks of dox treatment (“+dox”) and returned to the (“–dox”) baseline upon w/d (Fig. 1D), consistent with *XIST*-negative FISH in w/d samples (Fig. 1C).

To accurately measure chr21 dosage not only by standard differential expression analysis but also chr21 allelic representation, we additionally sequenced euploid and T21 whole genomes with linked reads to identify and phase variants. In both euploid and T21 iPSCs, most variants can be grouped in large phase blocks (N50 lengths of 1.8 and 2.9 Mb, respectively), including across chr21, where thousands of heterozygous variants distinguish the *XIST*-bearing (chr21^P) copy. To map mRNA-seq reads allele-specifically, we assigned variants to the chr21^P copy if their representation was lower in T21 than in disomic chr21 (D21) samples. These phased variants revealed that one allele was underrepresented with a mean lesser allele frequency (LAF) of one-third ($\frac{1}{3}$) for T21 samples. As suggested by the CytoSNP data (fig. S1), this is in keeping with the presence of a single chr21^P copy and two copies of chr21^{M/M2}, whereas the same chr21^P allele comprised about half of all allelic reads in the D21 samples (Fig. 2A). In the absence of dox (–dox), the *XIST*-bearing chr21^P copy (T21-*XIST*) still represented $\sim\frac{1}{3}$ of variant-mapping reads but was largely depleted in the +dox and w/d samples, the latter of which were dox-treated (3 weeks) and collected after another 3 or 6 weeks without dox. These data demonstrate that *XIST* silences most genes on the chr21^P copy near-completely, and irreversibly, consistent with our expectations based on mouse *Xist* reports, as reviewed in (25).

Likewise, differential expression analysis across chr21 reveals that nearly all genes with assessable expression were depleted by

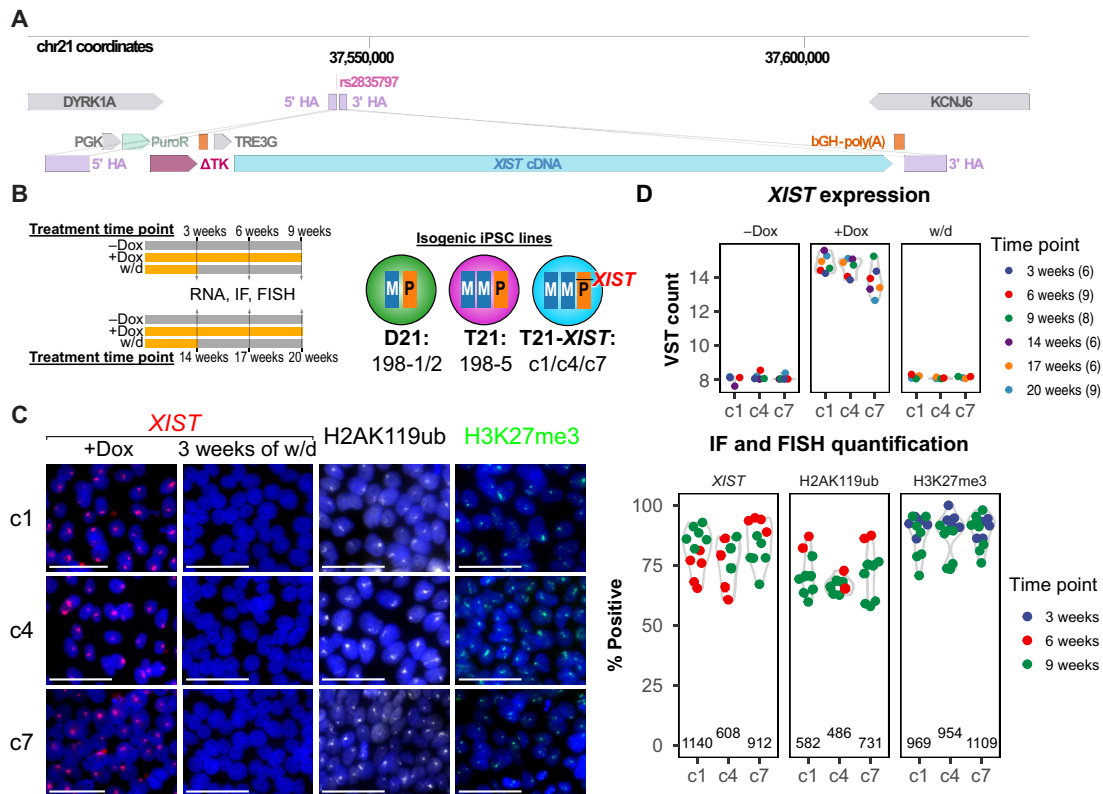


Fig. 1. T21 iPSCs induce *XIST* transgene and deposit heterochromatin on one chr21 allele. (A) A Tet-On 3G (TRE3G)-driven *XIST* cDNA is delivered to chr21 by homologous recombination using 5' and 3' homology arms (HAs) flanking rs2835797 (pink), which abrogates the protospacer motif of the Cas9 guide RNA on two of three alleles. Additional components include PGK-driven puromycin and thymidine kinase selection markers. Bovine growth hormone (BGH) polyadenylation [bGH-poly(A)] signals terminate the *XIST* cDNA and Puro-TK genes. (B) Schematic of iPSC sample collection time points and dox treatment conditions, alongside cell line names. Samples were collected after 3 to 9 weeks of +dox or no-dox treatment, or 3 weeks of +dox and 3 or 6 weeks of w/d. Another set of samples were collected at longer time points of 14 to 20 weeks of +dox or no-dox treatment or 14 weeks of +dox and 3 or 6 weeks of w/d. (C) Representative images (left; scale bars, 50 μ m) for *XIST*-FISH, H2AK119ub and H3K27me3 IF, and image quantification (right). Control panel of *XIST*-negative cells after 3 weeks of w/d for *XIST*-FISH included on the left. On right, each dot represents an individual image from a total of two time points (color) per clone and target. Total number of cells quantified for each clone and target annotated at bottom of panel. (D) *XIST* expression in T21-*XIST* samples from mRNA-seq (VST counts, approaching a log transformation). Total number of samples at each time point are noted in parentheses in "time point" color legend.

one-third [$\log_2(\text{fold change})$ ($\log_2\text{FC}$) of -0.59 ± 0.15] with D21 panels closely matching T21-*XIST* +dox and w/d panels, irrespective of their linear distance from the *XIST* transgene, and maintained that expression level even after 3 to 6 weeks of w/d (Fig. 2, B to D). Together, only a very small group of protein-coding genes appeared to retain significant chr21^P expression in the allelic analysis (Fig. 2A). In four of these genes (*ADAMTS1*, *H0Y3Z8*, and *IFNAR1/2*), representation of the chr21^P allele unexpectedly rose following *XIST* induction (+dox). This is most likely due to a few incorrectly phased variants that match on chr21^P and one chr21^M but consequently differ on the second chr21^M allele and, hence, cannot resolve the *XIST*-bearing chr21^P copy. All genes with an LAF of $\geq 1/6$ (*ADAMTS1/5*, *APP*, *H0Y3Z8*, *IFNAR1/2*, *MRPS6*, *ETS2*, and *YBEY*) were significantly down-regulated by the expected degree ($P \leq 0.1$, $\log_2\text{FC} = -0.59 \pm 0.15$), except for *IFNAR2* and the adjacent read-through open reading frame *H0Y3Z8*, which appeared to escape *XIST*-mediated repression by differential expression [adjusted P (P_{adj}) > 0.1]. To compare this efficacy to previously reported T21-*XIST* systems (24, 30), we considered the degree of silencing across all mutually assessed chr21 genes in a prior RNA-seq

study ($N = 150$), irrespective of adjusted P value cutoff, as our study included a greater number of samples. The distribution of $\log_2\text{FC}$ values in our T21-*XIST* indicates more complete gene repression than those in previously published datasets (fig. S2B).

Comparing differential expression in iPSCs after 3 and 6 weeks of w/d, we find that silencing was maintained in w/d samples, irrespective of the length of original dox treatment (Fig. 2B and fig. S2C). We therefore assessed DNA methylation (DNAm) at promoters, which reflects stable gene silencing known to remain intact even upon *Xist* deletion in mouse fibroblasts (48, 49). Excluding likely inactive promoters with high DNAm ($>60\%$ methylated), virtually all chr21 promoter-associated CpG probes of the MethylationEPIC array (Illumina) increased from a median of 7% methylated in -dox to 41% methylated after ≥ 3 weeks in +dox (Fig. 2F). This level is consistent with the presence of a fully methylated alongside two unmethylated alleles (one-third) and is maintained ≥ 3 weeks after w/d (39% methylated), which is also reflected in the absence of reactivated genes by differential and allelic expression (Fig. 2, A to E).

We next turned to transcriptome-wide effects of T21 and *XIST*-corrected gene dosage. While levels of chr21 genes clearly increased

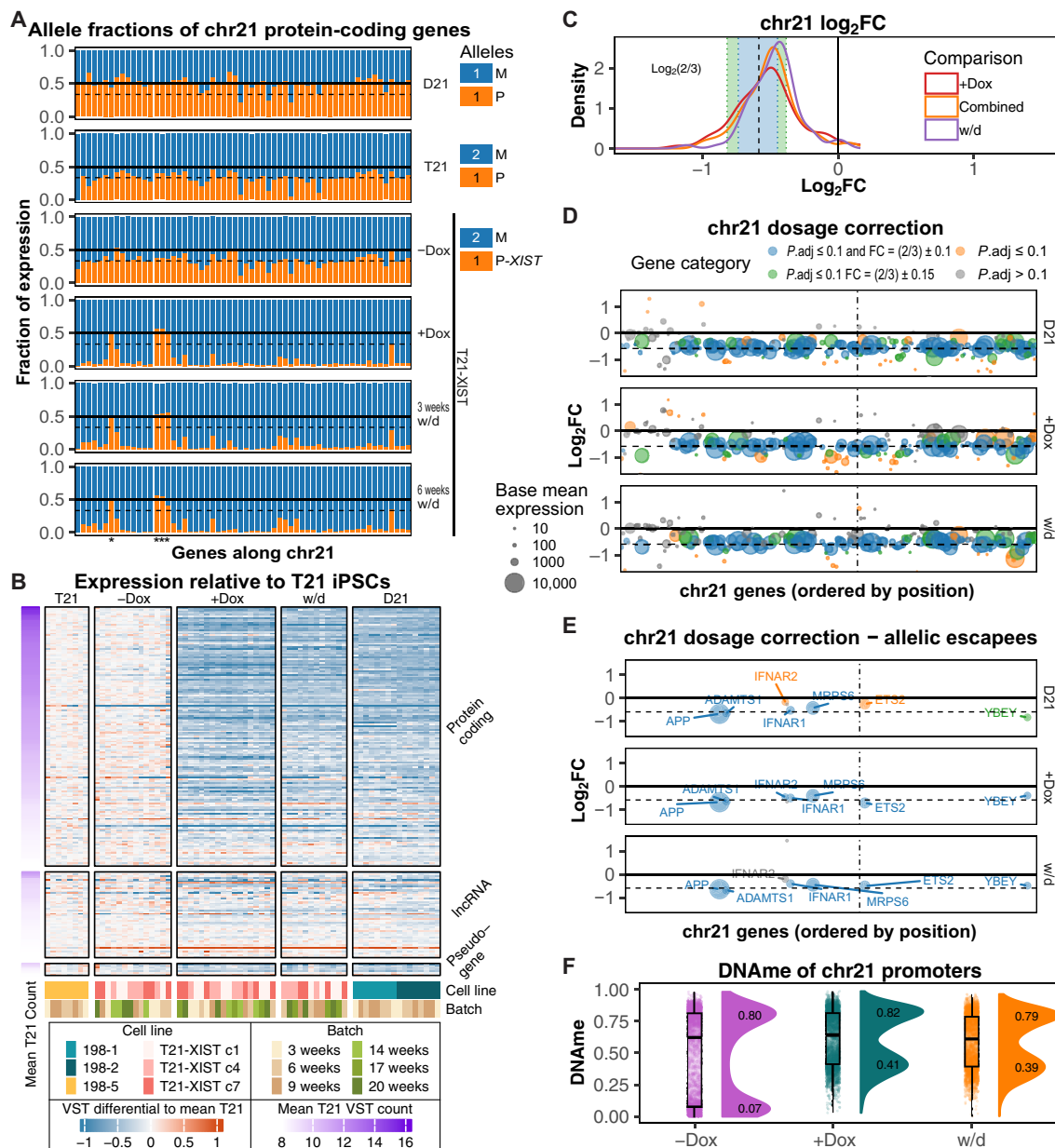


Fig. 2. XIST-mediated silencing extends across entire chr21^P and attracts DNAm. (A) Represented M/M2 and P alleles of protein-coding chr21 genes ($N = 60$) ordered along chr21 across dox conditions and genotypes (sample n : D21 = 16, T21 = 8, T21-XIST -dox = 14, +dox = 18, 3 weeks of w/d = 6, 6 weeks of w/d = 6). Thick black line at 0.5 marks expected biallelic expression in euploid (D21) cells, and dashed thin black line expected one-third representation for chr21^P allele in T21 cells. Asterisks denote genes with unresolved allelic origin. (B) Heatmap of VST differential of all samples ($n = 68$, cell line and batch denoted below) relative to the mean VST of T21 samples (left) for all expressed protein coding, long noncoding RNA (lncRNA), and pseudo-genes on chr21 ($N = 208$), ordered by VST count of T21 cells (violet annotation; left). (C) Distributions of \log_2FC of T21-XIST +dox ($n = 30$) and w/d ($n = 12$) samples relative to T21 samples ($n = 22$), for all genes with ≥ 1000 base mean expression ($N = 84$). "Combined" (T21-XIST +dox and w/d, $n = 30$) represents the differential expression condition used in subsequent figures as "T21-XIST/T21." Blue- and green-shaded bands indicate ± 10 and $\pm 15\%$ variations from a \log_2FC of -0.59 (dashed vertical line; expected \log_2FC of complete T21 dosage correction). (D) \log_2FC values across chr21 genes ($N = 131$ to 160 ; arranged by position) comparing D21, T21-XIST +dox, and T21-XIST w/d samples to T21 samples. Bubble colors are indicated in the legend above, and bubble size reflects base mean. (E) As in (B), displaying only genes that maintain an LAF $\geq 1/6$ in allelic T21 mRNA-seq under +dox or w/d conditions. (F) Distribution of DNAm values from promoter-associated methylEPIC probes on chr21 genes in T21-XIST no-dox, +dox, and w/d. Bimodal distribution medians of probes $>$ and $\leq 60\%$ methylated displayed on their respective peaks.

in T21 relative to D21 and decreased in T21-*XIST* +dox relative to -dox samples, all other chromosomes also responded to chr21 dosage (Fig. 3A). There was a small but significant bias ($P = 2.5 \times 10^{-7}$, binomial test) toward down-regulation in T21 iPSCs that disappeared when T21 dosage is corrected (fig. S3A and data S1). Consistently, samples with an effective chr21 dosage matching euploid

samples (D21 and +dox or w/d T21-*XIST*) (fig. S3B) segregated from T21 and no-dox T21-*XIST* samples in principal components analysis (PCA) (Fig. 3B). Because our experimental design included the original, nontransgenic D21 and T21 iPSCs (198-1/2/5) with all treatments (\pm dox and w/d), we were able to observe that their acute +dox treatment triggered expression changes that correlated, to

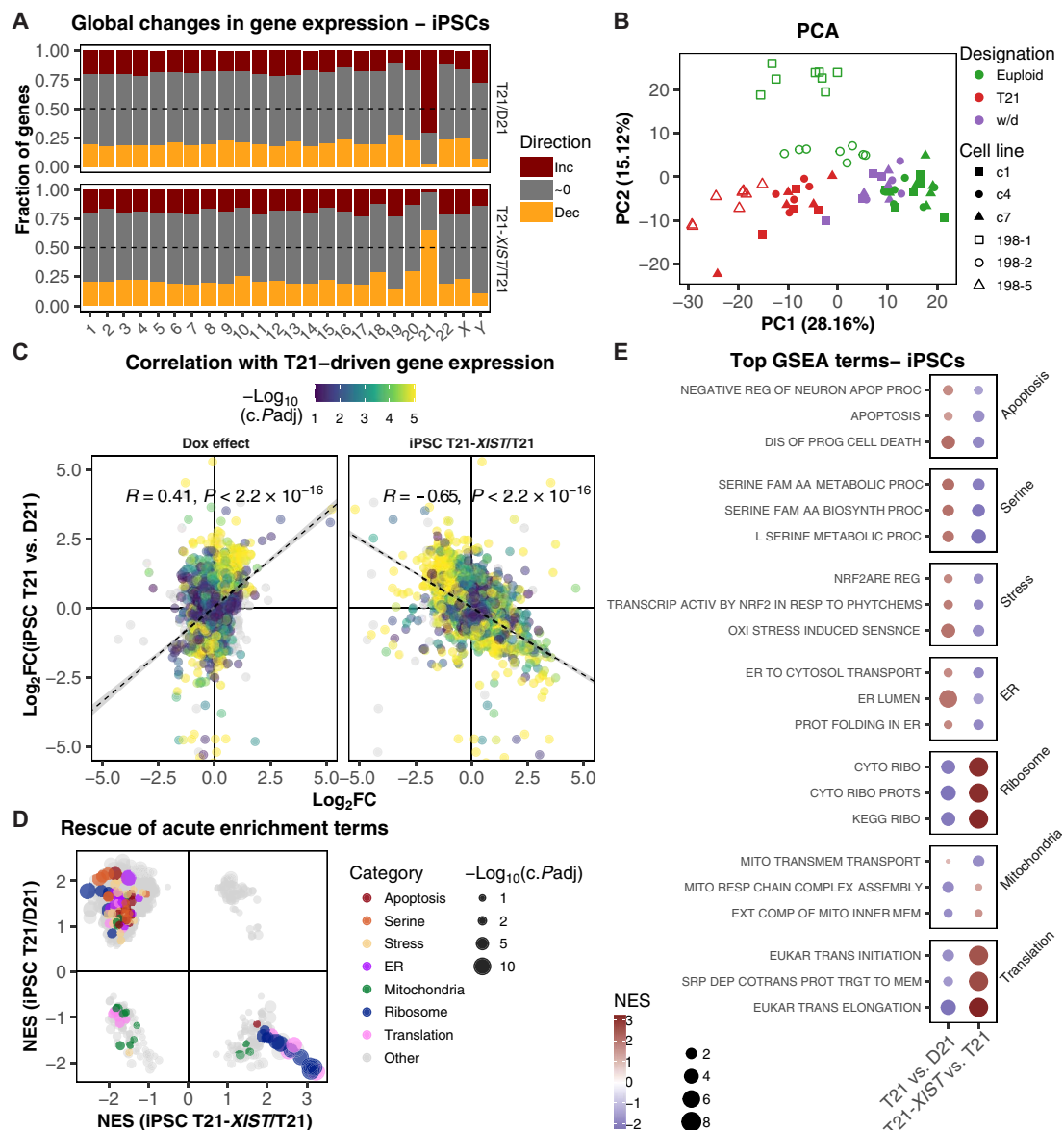


Fig. 3. Transcriptome-wide response to T21 gene dosage and correction via *XIST*. (A) Fraction of genes differentially expressed in response to T21 ($n = 22$) relative to D21 ($n = 16$) (top) and T21-*XIST* dosage correction ($n = 30$) relative to T21 (bottom), by direction (increasing, decreasing, or unchanged, ~0) and by chromosome. (B) Principal components analysis (PCA) of all mRNA-seq samples ($n = 68$) using all genes ($N = 18,929$), batch-corrected for time point and dox status. Open symbols denote original euploid (198-1/2) and T21 (198-5) lines, and filled symbols denote T21-*XIST* transgenic lines (c1/c4/c7). Colors indicate effective chr21 dosage as indicated in Figs. 1 and 2 (w/d colored separately to distinguish from +dox T21-*XIST* samples). (C) Overlap of differential expression between iPSC T21/D21 (y axis, $n = 22/n = 16$) over the dox effect (left; comparing only nontransgenic +dox, $n = 9$, and no-dox, $n = 15$) and T21-*XIST* dosage correction ($n = 30$) relative to T21 ($n = 22$). Adjusted P values combined by Fisher's method (c.Padj) for all DEGs and colored by $-\log_{10}(c.Padj)$ provided c.Padj ≤ 0.1 . Linear regression plotted with the Spearman correlation coefficient and P value for genes with c.Padj ≤ 0.1 (left, $N = 8417$; right, $N = 9396$). (D) Overlap of enriched GSEA terms comparing NES for iPSC T21/D21 ($n = 22/n = 16$) over dosage-corrected T21-*XIST*/T21 ($n = 30/n = 22$). Adjusted P values combined by Fisher's method (c.Padj) for all GSEA terms and shown as bubble size by $-\log_{10}(c.Padj)$. Colors denote terms within selected categories (c.Padj ≤ 0.2). (E) Individual significantly enriched terms (c.Padj ≤ 0.1) from each of the categories in (D), selected by concordance measure [Euclidean distance from origin in (D)]. Colors denote NES, and size denotes individual $-\log_{10}(P.adj)$.

some extent, with the T21 dosage effect (Fig. 3C, left), which was still significant after excluding chr21 genes from the correlation (fig. S3C, left).

This was not unexpected because dox can partially affect mitochondrial translation in eukaryotic cells (50) and mitochondrial pathways are also altered in DS (51–53). We therefore adjusted for this small dox-specific effect in our analysis (see Materials and Methods). We then compared T21 over D21 log₂FC expression changes with the combined (+dox and w/d) *XIST* correction, which revealed a highly significant and negative Pearson correlation of -0.65 (Fig. 3C, right) that persists even when chr21 genes are excluded (fig. S3C, right). These data indicate that differentially expressed genes (DEGs) responding to excess chr21 dosage are also changing in the opposite direction when excess chr21 dosage is corrected via *XIST*. This large-scale reversal was also evident in examining all pairwise comparisons of genome-wide variance-stabilized transformed (VST) counts from T21, D21, and dosage-corrected T21-*XIST* samples by analysis of variance (ANOVA). By this statistic, D21 and T21-*XIST* (+dox and w/d) samples exhibit minimal variability relative to either being compared to T21 samples, regardless whether chr21 genes are included or excluded (fig. S3D). Likewise, in gene set enrichment analysis (GSEA), normalized enrichment scores (NESs) of dosage-corrected T21-*XIST* relative to T21 and T21 relative to D21 enriched terms anticorrelated (Fig. 3D, top left and bottom right quadrants), many of which related to apoptosis, stress, endoplasmic reticulum (ER), mitochondria, and translation terms (data S2). Plotting the top three most concordant terms for each of these categories (Fig. 3E), T21 and dosage-corrected samples were near-uniformly opposed in biological processes previously implicated in DS, including apoptosis (17, 54), oxidative stress via NRF2 (16, 55), mitochondria (18, 51–53), and translation (14, 56). Serine biosynthesis pathways, recently attributed to a general response to aneuploidy (20), were also highly represented, indicating that serine metabolism returns to baseline upon T21 dosage correction, despite the continued presence of the supernumerary chr21 copy.

T21 gene dosage effects in mature neural cell types

To assess T21 gene dosage effects in neural lineages, we applied a well-established monolayer differentiation protocol that mimics in vivo neural development in the establishment of neurogenic niches (rosettes) and in the production of both mature neurons and astrocytes (57). We chose this approach as nearly all T21 iPSC-derived neuronal RNA-seq data reported to date was generated from relatively immature neurons. We performed mRNA-seq in 10 to 12 weeks of neural cultures, obtained 5 to 6 weeks after low-density replating of 4 weeks of NPCs (Fig. 4A). Relative to T21 neural cultures, euploid and T21 dosage-corrected (+dox and w/d) samples showed reduced chr21 transcript levels with a peak near the expected -0.59 log₂FC relative to euploid samples (Fig. 4B). As seen in T21 dosage correction in iPSCs (Fig. 3), neural DEG log₂FC and NES values of GSEA-enriched terms in T21 over D21 comparison anticorrelated ($R = -0.61$, $P \leq 2.2 \times 10^{-16}$) with those of the combined T21-*XIST* correction (+dox and w/d) over T21 comparison (Fig. 4, C and D), which also extended to the three most concordant terms across all comparisons (Fig. 4E). Overall, we find that *XIST*-mediated T21 dosage correction is reflected in a majority of significantly enriched terms of T21 iPSCs and differentiating neural cultures compared to euploid controls (fig. S4 and data S1 and S2).

To assess whether the number of overrepresented GSEA terms relating to cell death and apoptosis in T21 neural cultures manifested in differential neuronal survival, we used a recently developed a ratiometric red genetically encoded cell death indicator (RGEDI) to track two neuronal populations by automated longitudinal imaging (Fig. 5A and fig. S5) (58, 59). Subtypes of cortical interneurons are reportedly vulnerable to T21 dosage (60), but increased cell death had been reported only in heterogenous T21 neuronal populations to date (17, 31, 33, 54, 61, 62). While these differentiation methods, referred to as “forebrain” protocols, mainly generate excitatory, glutamatergic neurons (63), ventralizing sonic hedgehog agonist (64, 65) drives human iPSC-derived NPCs to differentiate to a population enriched for GAD67⁺ γ -aminobutyric acid (GABAergic)-releasing interneurons (fig. S5A). Both T21-derived interneurons (hazard ratio of 4.08) and excitatory forebrain neurons (hazard ratio of 2.57) demonstrated significantly increased cell death [RGEDI/enhanced green fluorescent protein (EGFP) ratio > 0.15 , Holm-corrected $P < 0.01$, linear mixed model] over ~10 days of single-cell tracking, compared to their isogenic euploid controls (Fig. 5, B and C). In addition, we also assessed live neurons (RGEDI/EGFP ratio < 0.15) and noted that there was a significant ($P \leq 10^{-8}$) reduction in EGFP signal in T21 compared to euploid controls (fig. S5F), which mirrored the down-regulation of ribosome and translation-related GSEA terms in both T21 iPSCs and neural cultures (Figs. 3 and 4 and fig. S4).

T21 dosage correction early in neural differentiation rescues neurogenesis

Assessing neural cell fate decisions, we observed an excess of astrocytes (S100B marker) in T21 relative to predominantly neuronal (MAP2 marker) euploid neural differentiations, in both early and mature neural populations (fig. S6A). Both neurons and astrocytes derive from NPCs (66), and astrogliosis has been reported in DS models (36, 37) and fetal samples (31, 33, 35), where T21 NPCs prematurely shift from neurogenesis to astrogenesis. To determine whether *XIST*-mediated T21-dosage correction could prevent this lineage skew, we first confirmed that *XIST* expression and H2AK119ub enrichment would persist in 4 week NPCs, which was the case for well over 75% of NPCs derived across three independent clones, treated with +dox as iPSCs (Fig. 6A). Even NPCs derived from untreated T21-*XIST* iPSCs but receiving dox from the first day of differentiation (“d0”) presented with *XIST* and H2AK119ub foci in $\geq 75\%$ and $\geq 65\%$ of all cells, respectively. Costaining for MAP2 and S100B early in neural differentiation following terminal plating of d28 NPCs revealed a consistent and highly reproducible primary astrogenic skew in T21 and no-dox T21-*XIST* samples relative to isogenic euploid control lines across multiple rounds of differentiation (Fig. 6, B and C). Neurogenesis was fully rescued in neural differentiations from pretreated and d0 +dox-treated iPSCs, across all three independent T21-*XIST* clones. Because the overall sum of committed cells expressing either marker did not differ significantly between T21 and euploid or T21-*XIST* dosage-corrected samples, we propose that T21 dosage does not suppress NPC commitment in general, as previously suggested (30), but rather advances the shift to astrogenesis, which is consistent with reports in fetal DS and rodent DS models (33, 37).

To test whether this interpretation is replicated in vivo, at the very onset of cortical astrogenesis, we turned to the Ts(17¹⁶)65Dn (Ts65Dn) model (fig. S6, B and C). At embryonic day 18.5 (E18.5), the density of S100B⁺ astrocytes in the developing cortex was significantly elevated

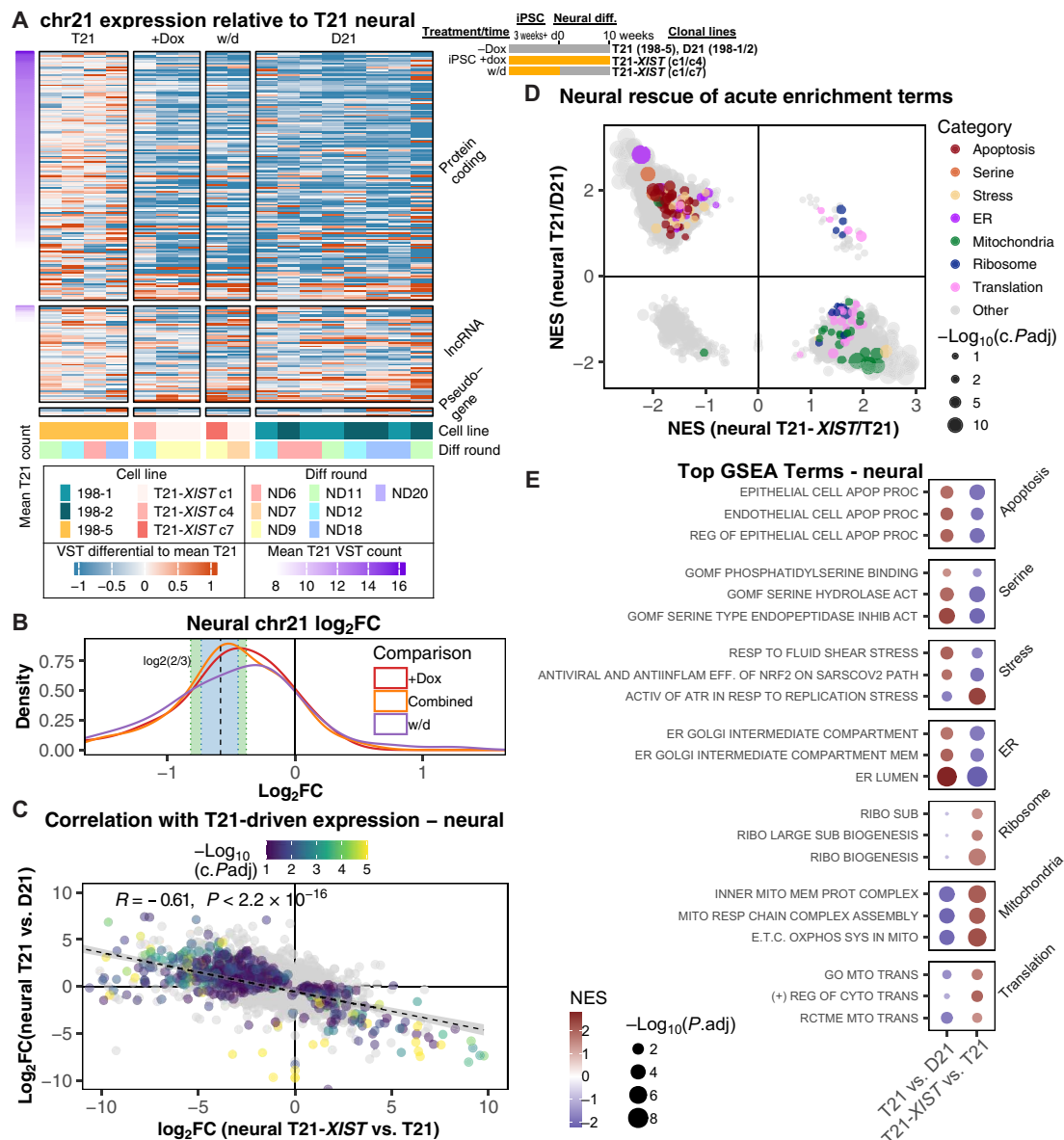


Fig. 4. Concordant T21 dosage imbalance and transcriptomic response after neural differentiation. (A) Heatmap of VST differential for each sample ($n = 17$) relative to the mean VST of all T21 neural samples (left) for all expressed protein-coding, long noncoding RNA, and pseudo-genes on chr21 ($N = 213$). Schematic (right) details dox conditions, neural differentiation end point, and cell lines. (B) Distribution of log₂FC relative of +dox ($n = 3$) and w/d ($n = 2$) to neural T21 samples ($n = 4$), for all genes with ≥ 1000 base mean expression ($N = 86$). Combined ($n = 5$) represents the differential expression condition used in subsequent figures as T21-XIST/T21. Blue- and green-shaded bands correspond to ± 10 and $\pm 15\%$ variation from a log₂FC of -0.59 (dashed vertical line; log₂FC expected for complete T21 dosage correction). (C) Overlap of differential expression between neural T21/D21 (y axis; $n = 4/n = 8$) and T21-XIST (y axis; +dox and w/d, $n = 5$) relative to T21 ($n = 4$). Adjusted P values combined by Fisher's method ($c\text{-}Padj$) for all DEGs and colored by $-\log_{10}(c\text{-}Padj)$ provided $c\text{-}Padj \leq 0.1$. Linear regression plotted with the Spearman correlation coefficient and P value for genes with $c\text{-}Padj \leq 0.1$ ($N = 586$). (D) Overlap of enriched GSEA terms comparing NESs for neural T21/D21 (y axis) to NES for dosage-corrected T21-XIST/T21 (x axis). Adjusted P values combined by Fisher's method ($c\text{-}Padj$) for all GSEA terms and shown as bubble size by $-\log_{10}(c\text{-}Padj)$. Colors denote terms within selected categories with $c\text{-}Padj \leq 0.2$. (E) Individual significantly enriched terms ($c\text{-}Padj \leq 0.1$) from each of the categories in (D), selected by concordance measure [Euclidean distance from origin in (D)]. Colors denote NES, and size denotes the individual $-\log_{10}(P\text{-adj})$.

in Ts65Dn embryos over their wild-type littermates ($P < 0.05$). In contrast, there was no significant difference in the density of cycling Ki67⁺ cells in the proliferative zone (fig. S6), indicating that the early cortical astrogenesis in Ts65Dn embryos was not associated with delayed commitment of neural progenitors but, rather an inherent skew toward astrogenesis also observed in other brain regions (33, 37).

Postmitotic neural cell types still induce *XIST* and attract repressive chromatin marks

Given the high rate of *XIST* induction in T21-XIST NPCs that only received dox at the onset of differentiation (d0), we next explored whether the *XIST* transgene would remain dox-responsive in terminally differentiated cells (Fig. 7A). To this end, we forced NPCs

out of the cell cycle into terminal differentiation by inhibiting the Notch signaling pathway for 5 days with γ -secretase inhibitor DAPT and added dox a day after completing DAPT treatment (d33). To confirm that DAPT treatment was sufficient to deplete mitotic cells, we also labeled cells transiting S phase with nucleotide analog 5-ethynyl-2'-deoxyuridine (EdU) (Fig. 7B) and costained for this label and *XIST* FISH after 2 days in +dox medium (d35).

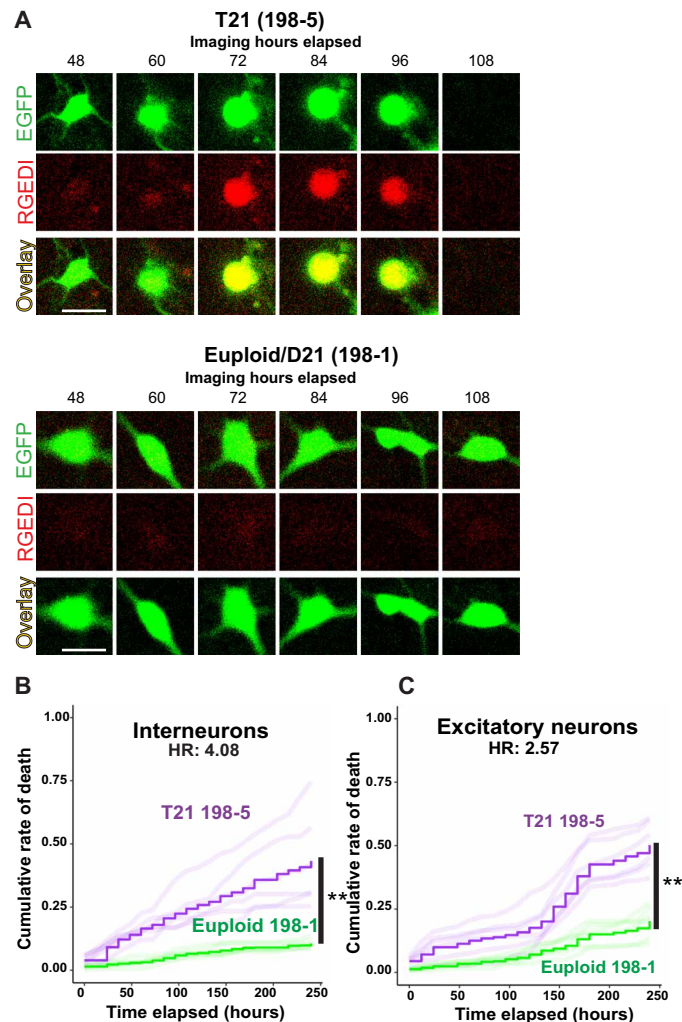


Fig. 5. Increased cell death of T21 relative to euploid interneurons and excitatory forebrain neurons. (A) Representative sequence of a T21 interneuron labeled with RGEDI-P2a-EGFP dying over the course of imaging and a control neuron surviving during the course of imaging (scale bar is 10 μ m). The colors of the cells in red and green directly correspond to the “red indicator RGEDI” and “EGFP” morphology, respectively, as these images were captured using red fluorescent protein and green fluorescent protein channels. The two labeled channels are in separate panels and also presented as overlays (yellow), while maintaining the color scheme in the manuscript to ensure clarity and coherence. (B) Plot of the cumulative rate of death of T21 (707 cells) and euploid control interneurons (1092 cells). Step functions correspond to the mean cumulative death rate across all wells per line, and the faint lines represent cumulative death rate of each replicate well ($n = 6$ wells each, hazard ratio (HR) = 4.08, linear mixed model with Holm correction, $**P < 0.01$). (C) As in (B) for the cumulative rate of death of T21 (1953 cells) and euploid control (1151 cells) excitatory forebrain neurons ($n = 6$ wells each, HR = 2.57, linear mixed model with Holm correction, $**P < 0.01$).

DAPT-treated NPCs incorporating EdU comprised $\leq 7\%$ of the neural population on average, which were rarely EdU/*XIST* double-positive ($\leq 2\%$ overall), whereas *XIST* was induced in $\geq 40\%$ of all cells. We conclude that *XIST* was reliably induced in a sizeable fraction of postmitotic T21-*XIST* cells that had terminally differentiated without dox. We next assessed these postmitotic cells after 3 to 6 weeks of dox treatment post-DAPT (“pD”) exposure to provide sufficient time for H2AK119ub enrichment. We included d0 controls that were treated with the standard 1 μ M dox concentration throughout neural differentiation, as well as low-dose “LD” dox samples, which were treated with 0.01 μ M dox up to the DAPT exposure and standard 1 μ M dox thereafter (Fig. 7A), to test whether “premarking” the TRE3G promoter without effective induction through differentiation may render it more responsive in terminal cell types. On average, over half of d0 and LD cells featured prominent *XIST* clouds, followed by $\geq 40\%$ of pD samples, across both T21-*XIST* clones (c1 and c7) and in three independent rounds of differentiation. As before, H2AK119ub signal lagged slightly behind *XIST* but consistently marked 27 to 36% of all cells (58 to 65% of *XIST*⁺ cells), including MAP2⁺ neurons and S100B⁺ astrocytes (Fig. 7, C and D).

XIST induction in terminal neurons and astrocytes corrects T21 gene dosage

We next performed single-nucleus RNA-seq to determine whether *XIST* induction and H2AK119ub accumulation in these terminally differentiated neural cell types reflect T21 dosage correction (Fig. 8). Transgenic neural differentiations treated with dox from d0 or pD were collected alongside untreated T21-*XIST* c7 cells (“T21”) and two euploid lines (198-1/2 or “D21a/b”). Nuclei distributed across four broad clusters, of which three corresponded to the expected NPC, neuronal, and astroglial populations (Fig. 8A and fig. S7A). Cell cycle analysis classified the smaller NPC cluster as S and G₂-M phase cells, while all other clusters scored as G₁, consistent with terminally differentiated G₀ cells (Fig. 8A and fig. S7A). We labeled the first three clusters according to their predominant cell type using cell type markers from (67) and the fourth as “other” given lower scores returned by scType (68). Because of its proximity to higher-scoring oligodendroglial progenitor cells (OPCs), this fourth cluster probably reflects OPC-derived lineages that predominantly arose from one of the euploid lines (D21a). Crucially, *XIST* induction in T21-*XIST* neural differentiations (d0 and pD) was detected in all clusters with 74 to 94% of d0 +dox-treated and 24 to 58% pD +dox-treated cells (fig. S7A), in agreement with our FISH and IF data (Fig. 7).

To determine whether *XIST* induction repressed T21 gene dosage, we assessed three complementary metrics. First, we phased single-nucleus RNA-seq reads and summed allele-specific counts across all chr21 genes to calculate the cumulative paternal allele representation (Fig. 8B), thereby mitigating the effect of transcriptional bursts in individual nuclei (69). As expected, euploid cells have a significantly higher chr21^P allele fraction compared to T21 cells (0.46 versus 0.32; Wilcoxon, $P = 1.6 \times 10^{-11}$), whereas T21-*XIST* d0 +dox-treated cells have a significantly lower chr21^P allele fraction (0.14; Wilcoxon, $P < 2.2 \times 10^{-16}$). Crucially, while *XIST*-negative pD (pD-X⁻) cells show little reduction in this *XIST*-carrying paternal allele, *XIST*-positive pD (pD-X⁺) cells reveal significant repression of this allele (0.19; Wilcoxon, $P = 1.3 \times 10^{-12}$). Separating cells by cell type group (fig. S7B) reveals that *XIST*⁺ d0 and pD neurons repress the transgene-bearing chr21^P copy most robustly, with

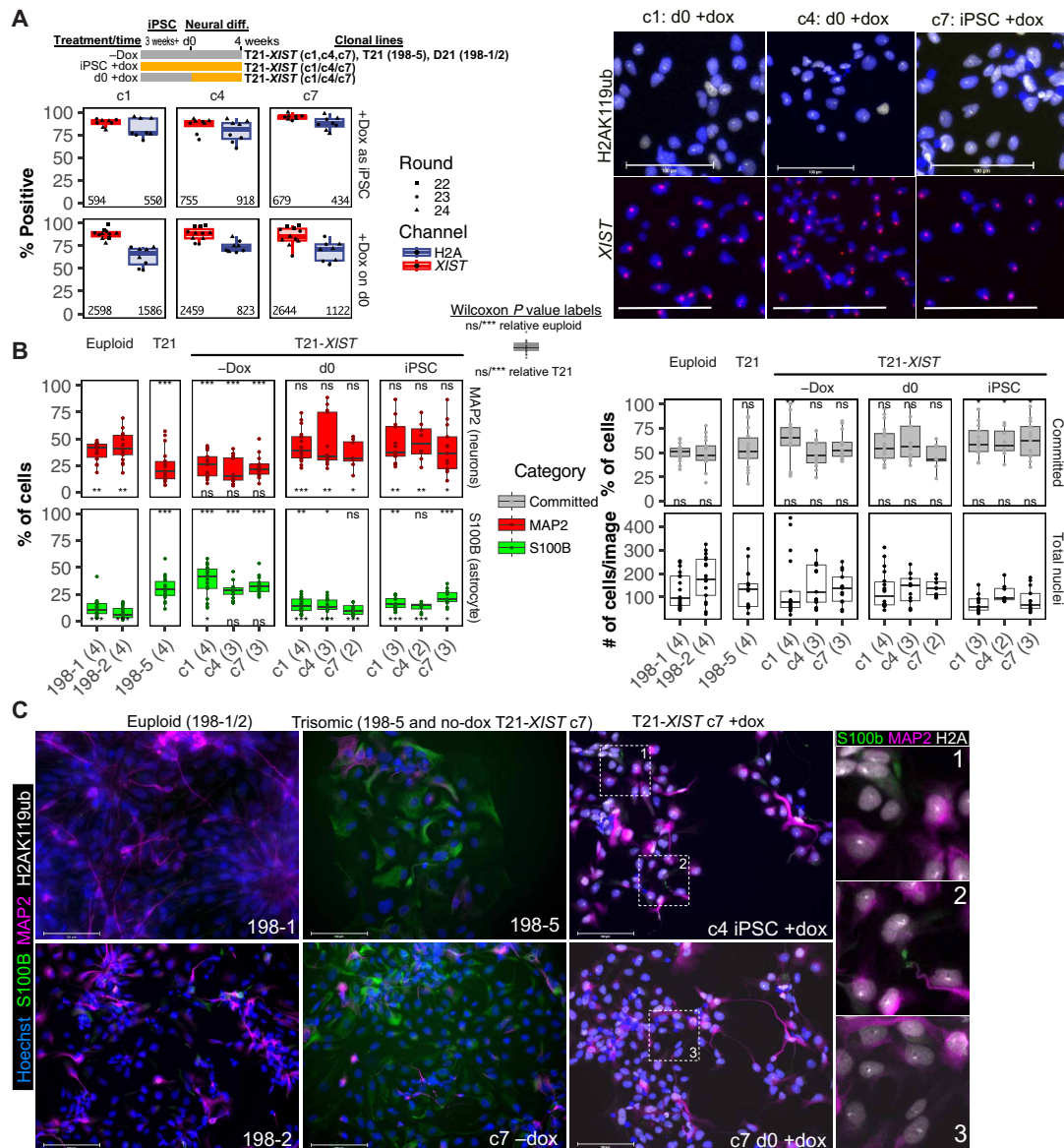


Fig. 6. Early astrogenesis at neurogenic expense is suppressed by T21 dosage correction before NPC stage. (A) Schematic details dox conditions, differentiation timeline, and cell lines used in assessing the impact of T21 dosage correction on reversing neural cell lineage bias. Quantification (left; data points indicate images and numbers of the total of scored cells across three replicate rounds of differentiation) and representative images (right; scale bars, 100 μ m) of H2AK119ub (IF) and *XIST* (FISH) signal after neural differentiation. Cells were dox-treated as iPSCs (top left) or d0 (bottom left). (B) Relative lineage commitment to neurons (MAP2; top left) or astrocytes (S100B; bottom left) in euploid, T21, and T21-*XIST* upon terminal plating of d28 cells. Symbols (two-tailed Wilcoxon *P* value level, $*P \leq 0.1$, $**P \leq 0.01$, $***P \leq 0.001$, or "ns" for $P > 0.1$) above each box plot denote significance of median difference from the corresponding euploid (198-1/2) condition, whereas symbols below each box plot compare to T21 (198-5) lineage proportions. Fraction of all committed cells (top right) shows the sum of neurons and astrocytes. Total number of cells counted in each image (bottom right). Replicate rounds of differentiation indicated for each cell line and dox condition (x axis). Data points represent individual images. (C) Representative images 3 weeks after terminal plating of d28 cells (scale bars, 100 μ m; 198-1: scale bar, 50 μ m) in euploid (left), T21 (center), and dosage-corrected T21-*XIST* (right; with dox addition time point) detecting nuclei (blue; Hoechst), neuronal MAP2 (magenta), astroglial S100B (green), and H2AK119ub accumulating on chr21 (white). Insets (labeled 1 to 3) display H2AK119ub foci in astrocytes and neurons.

paternal allele fractions of 0.15 and 0.17 (Wilcoxon, $P < 10^{-4}$), respectively.

Second, we compared the normalized expression for each gene on chr21 to the genome-wide mean without chr21. We then determined the per-cell cumulative distribution of all chr21 genes, as well as the per-gene cumulative distribution by cell type group (fig. S7, C and D), and aggregated these ratios across all neurons, astrocytes,

and NPCs (Fig. 8, C and D). Euploid and T21-nodox medians fell near the expected 1.0 \times and 1.5 \times ratios relative to the genome-wide mean (Fig. 8, C and D), consistent with our bulk RNA-seq results (Figs. 2 and 4) and the notion that chr21 genes are not inherently dosage-compensated at the transcript level (70). Likewise, pD-X⁻ nuclei failed to differ significantly from the T21-nodox sample (1.5 \times and 1.3 \times for the per-cell and per-gene ratios, respectively). *XIST*⁺

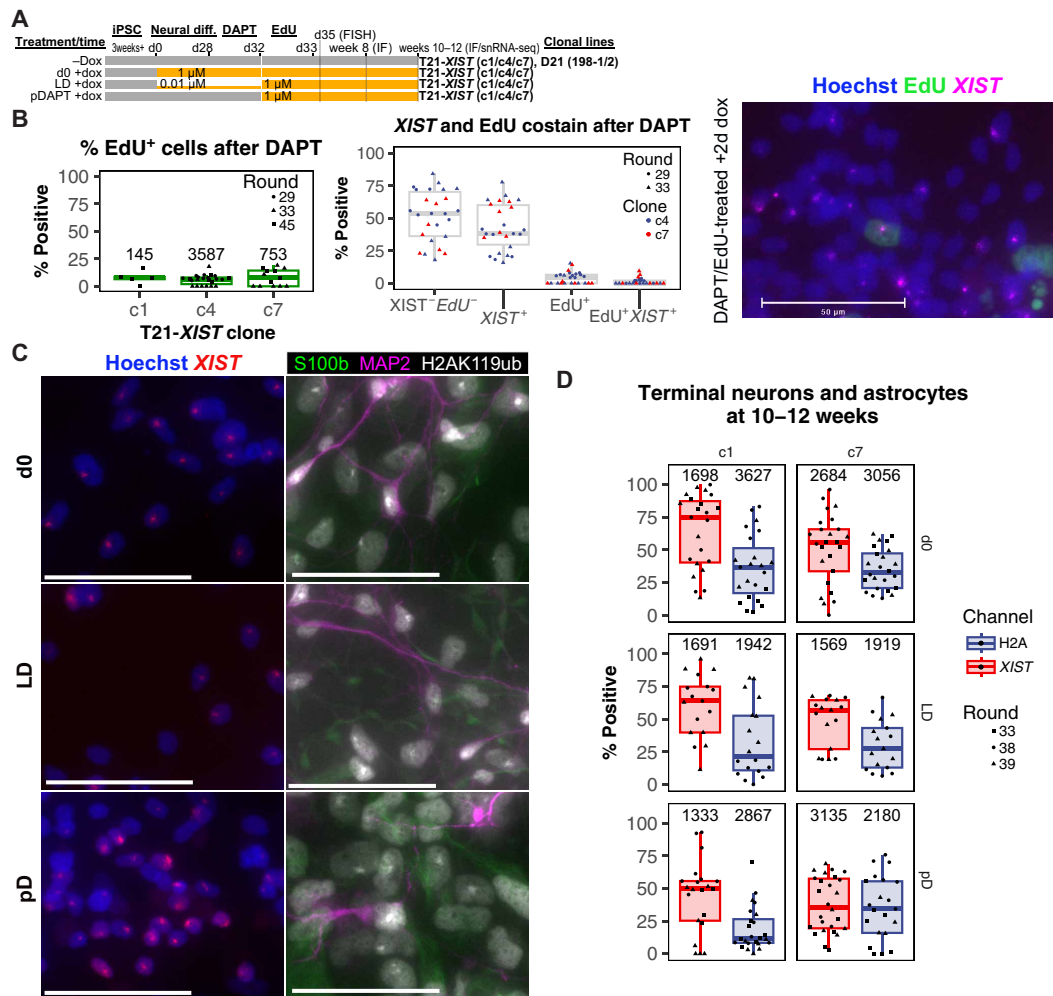


Fig. 7. Postmitotic neurons and astrocytes induce *XIST* and deposit H2AK119ub after lineage commitment. (A) Sample and timeline schematic of T21-*XIST* induction during (d0 +dox) and after terminal neural differentiation via DAPT treatment (d28 to d32), with LD pre-DAPT dox treatment (LD +dox) or without (pD +dox). Cell cycle exit of NPCs is assessed by EdU labeling of S phase-transiting cells, with codetection of *XIST* by FISH after 2 days +dox. Chr21 Barr body formation (H2AK119Ub) and lineage commitment (MAP2/S100B) are assessed by IF in 8 and 10 to 12 weeks of cultures, and snRNA-seq (single nucleus RNA-seq). (B) Quantification of EdU-labeling efficiency (left), EdU/*XIST* codetection (middle), and representative *XIST* (magenta) and EdU (green) image (right; scale bar, 50 μ m) at d36 of neural differentiation following DAPT (4 days) and dox treatment (2 days). Number of total nuclei counted noted above box plots in EdU-labeling efficiency. For EdU/*XIST* codetection, clones (color) and differentiation rounds (shape) are noted, and each data point represents an image. The composition of all cells counted ($n = 2816$) across both clones and rounds of differentiation is $XIST^+EdU^+ = 1.8\%$, $XIST^+ = 40\%$, $EdU^+ = 5.1\%$, and $XIST^-EdU^- = 53\%$. (C and D) Representative images (C) (scale bars, 100 μ m) and quantification (D) of H2AK119ub (white) IF and *XIST*-FISH (red) signals after neural differentiation from different dox treatments. Number of cells counted noted above box plots in (D). IF panels in (C) show H2AK119ub (white) costained with MAP2 (magenta) and S100B (green).

pD nuclei, however, displayed near-euploid chr21 dosage medians (ratio of $1.1\times$ and $1.0\times$; Wilcoxon, $P \leq 2.4 \times 10^{-7}$), very close to d0 nuclei (Fig. 8, C and D). Separated by cell type group, neurons again demonstrated near-complete dosage compensation in $XIST^+$ pD nuclei with median ratios of $0.97\times$ and $0.92\times$ on a per-cell and per-gene bases, respectively (Fig. 8, C and D). Assessing both metrics across full distributions for each sample, the pD- X^- distribution tracked closely with T21-nodox cells, remaining well within its 95% confidence interval. In contrast, the $XIST^+$ pD and d0 distributions shifted to the left significantly (dashed lines; Kolmogorov-Smirnov test P values) toward the euploid distributions for all cell type groups, irrespective of whether normalized expression ratios were averaged over cells or genes (fig. S7, C and D). Aggregating these

distributions across astrocytes, neurons, and NPCs illustrates $XIST^+$ d0 and pD nuclei tracked on top of each other, with their 50% percentile ratios near-identical to euploid nuclei (fig. S7, E and F). In sum, these data indicate that *XIST* corrects T21 gene dosage in postmitotic cell types via robust repression its chr21^p copy, especially in neurons, whereas NPCs mitigate *XIST*'s impact to some extent, possibly due to continued passage through M phase.

As our third metric for T21 dosage correction, we performed differential expression analysis on variance-stabilized data (71) and compared effectively trisomic (pD- X^- and nodox) nuclei to euploid (D21a/b), $XIST^+$ pD, and d0 nuclei for each cell type (data S3). In general, lower expression of chr21 in euploid relative to trisomic nuclei was also observed for $XIST^+$ pD and d0 nuclei (fig. S7G).

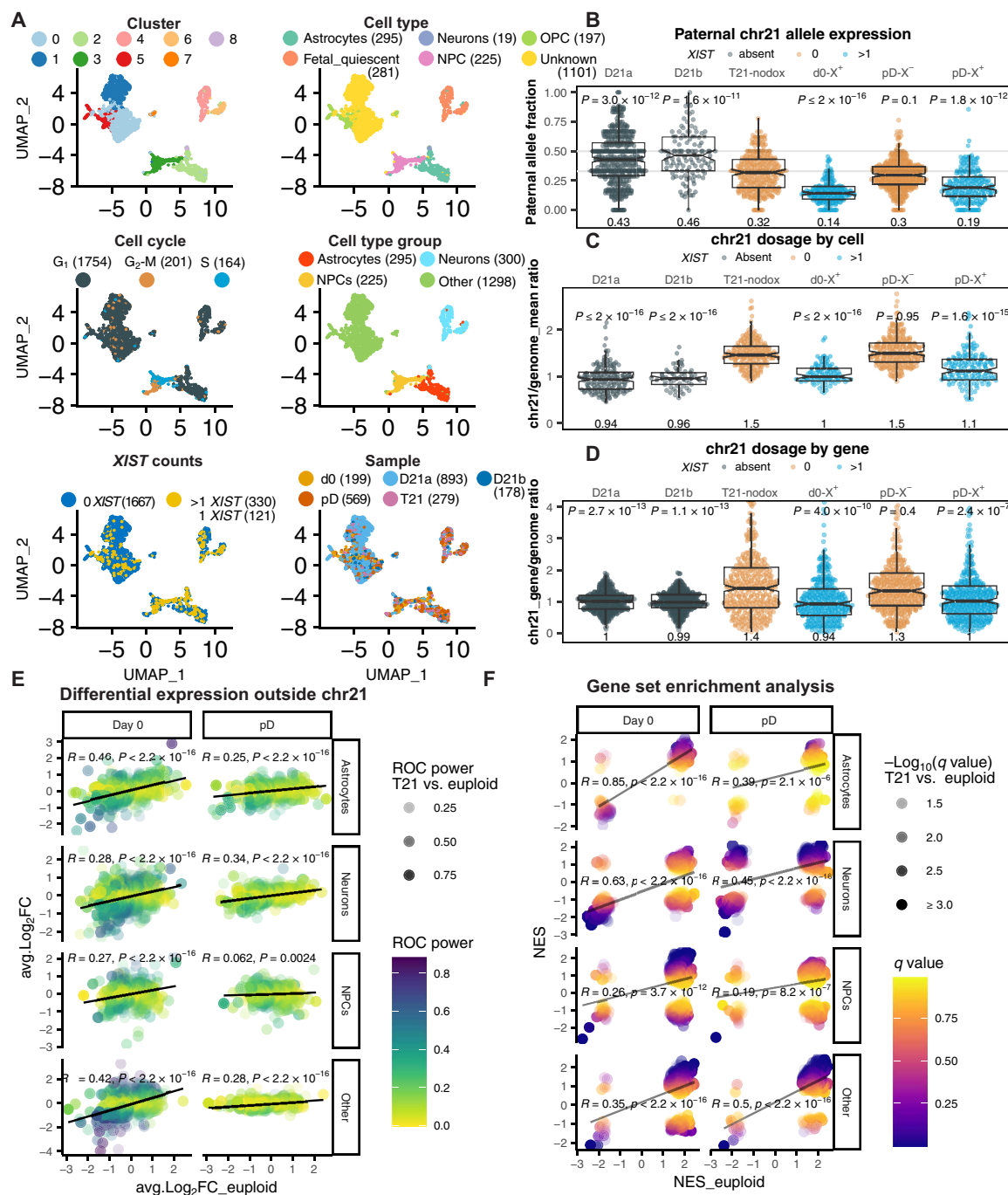


Fig. 8. Effective monoallelic repression of chr21 genes by XIST induced in terminal neurons and astrocytes. (A) Single-nucleus RNA-seq Uniform Manifold Approximation and Projection (UMAP) of terminal 10 to 12 weeks of neural cultures (integrating $n = 2118$ cells on $N = 3000$ genes) colored by original clusters, granular and grouped cell types, cell cycle stage, XIST counts, and samples (n cells per category in parentheses). (B) Paternal allele fraction by cell, aggregated over all chr21 genes. Cells split by sample (D21a/b, T21-XIST-nodox, d0+dox, and pD+dox) and XIST status (0, >1 counts denoted "X⁻" and "X⁺"), except for euploid lines (transgene absent; gray). Median paternal allele fraction and significance of median differences relative to T21-nodox cells (Wilcoxon P value) denoted below and above box plot, respectively. (C) Normalized expression ratio (over genome mean excluding chr21) by cell, aggregated over all chr21 genes. Cells split as in (B) (excluding other cells), with median expression ratio and difference in medians relative to T21-nodox cells (Wilcoxon P value) denoted above and below box plot, respectively. (D) Normalized expression ratio by chr21 gene relative to their mean euploid expression aggregated over cells. Mean ratios per gene calculated from cells split and annotated as in (C). (E) Differential expression of non-chr21 genes relative to pD-X⁻ and T21-nodox cells. Sample-averaged log₂FC values in euploid cells (x axis) correlate with XIST-positive d0 and pD log₂FC values (y axis) by cell type group. Colors denote ROC (receiver operating characteristic) power and transparency ROC power comparing euploid to T21 cells. Regression line (black), Pearson coefficient, and P value (Fisher-transformed) are shown as indicated. (F) GSEA results of expression comparisons in (E), correlating NESs, and plotted as in (E). MSigDB gene sets limited to Hallmark and canonical pathways significant ($q \leq 0.1$) in T21/euploid comparison (x axis). Log₁₀-transformed q values denoted by color (d0 and pD to T21) and transparency (euploid to T21). Regression line (gray), Pearson coefficient, and P value (Fisher-transformed) are shown as indicated.

Because of greater dispersion inherent in single-nucleus RNA-seq, the moderated effect sizes (avg.log₂FC) reflected in variance-stabilized data were smaller than in our bulk RNA-seq (Figs. 2 and 4) but enabled comparing euploid to *XIST*-corrected T21 gene dosage. *XIST* repressed chr21 genes to the near-euploid median, in all except other cell types, which showed a small but significant residual excess expression (Wilcoxon, $P = 0.0007$; fig. S8A). While the linear distance to the *XIST* transgene integration site did not correlate with mean log₂FC values in any of the d0 +dox cell types, there was a distance effect in pD +dox neurons and NPCs (fig. S8, B and C).

Differential expression of non-chr21 genes in *XIST*⁺ d0 and pD nuclei correlated strongly with log₂FC values in euploid relative to effectively trisomic nuclei across all cell type groups (Fig. 8E), with Pearson coefficients ranging from 0.25 to 0.46 in all except *XIST*⁺ pD NPCs. GSEA also reflected this transcriptome-wide reversion with strong NES correlations between *XIST*⁺ d0, pD, and euploid conditions in MsigDB Hallmark and canonical pathways that were significantly enriched ($q \leq 0.1$) in euploid relative to effectively trisomic nuclei (Fig. 8F). Again, the correlation in NPCs was the lowest across all cell type groups, yet still significant ($R = 0.19$, $P = 8.2 \times 10^{-7}$). The vast majority of MsigDB Hallmark and canonical pathways significantly enriched in any pairwise comparison (combined Fisher's method, $P \leq 1 \times 10^{-4}$) followed the direction of change in the remaining third comparison (fig. S8D and data S4). In sum, these results indicate that the degree of chr21 dosage correction in *XIST*⁺ d0 and pD nuclei is sufficient to revert T21 cells toward the euploid expression profile. We conclude that this new T21-*XIST* transgene corrects chr21 dosage even in terminal and postmitotic cell types, which will facilitate detailed exploration of cellular and transcriptional T21 hallmarks that remain reversible after completed development.

DISCUSSION

The relevance of the inducible T21-*XIST* system presented herein ranges from DS biology and cellular responses to aneuploidy in general, to fundamental questions relating to human *XIST*-mediated gene silencing and escape. In iPSCs, our T21-*XIST* system is induced with near uniformity (Fig. 1) and corrects T21 dosage to euploid levels across chr21 (Fig. 2), which we demonstrate by inclusion of isogenic euploid control iPSCs lines that we derived in parallel from a male donor with mosaic T21 (39). Leveraging phased sequence variants from linked-read whole-genome sequencing (WGS), we can assign mRNA-seq reads allele-specifically to show that chr21 genes derive half of their expression from the chr21^P allele in euploid (D21) cells and one-third in T21 cells but nearly extinguish expression from this *XIST*-bearing copy after dox induction (Fig. 2).

XIST-mediated T21 dosage correction extends to genes responding to chr21 dosage on all chromosomes, reflecting a transcriptome-wide reversion of gene expression that moves dox-treated T21-*XIST* iPSCs toward their isogenic euploid controls (Fig. 3). A balanced experimental design and stability of T21 silencing after w/d enabled us to adjust for dox effects that can inhibit mitochondrial translation (50) and selenocysteine incorporation (72). GSEA reflects the large-scale reversion of T21-responsive cellular components, pathways, and functions (Fig. 3), including boosted expression of serine biosynthesis genes. These genes are notable as dermal fibroblast of DS, as well as Patau (T13) and Edwards (T18) syndromes, depend on

serine for proliferation (20). As these genes return to baseline upon correction of T21 dosage (Fig. 3) despite maintenance of three chr21 copies, metabolic demand for serine, while common to all three viable human autosomal aneuploidies, results from expression of the supernumerary chromosome rather than its presence. We also find resurgent expression of ribosomal protein genes and translation factors in T21 dosage-corrected iPSCs (Fig. 3), which may be due to a resetting of the integrating stress response (14). Cellular stress pathways and apoptosis are dampened in response to T21 dosage correction, which is consistent with the previously reported excess of cell death (17, 31, 33), mitochondrial dysfunction (18, 51–53) and oxidative stress (16, 55) in DS.

In T21-driven expression of neural cultures, we find many of the same terms are enriched by GSEA (Fig. 4 and fig. S4). Induction of *XIST* prior to or at the onset of neural differentiation of T21-*XIST* cells efficiently represses T21 dosage and reverts neural gene expression profiles and GSEA term enrichment (Fig. 4 and fig. S4), mirroring what we observe in iPSCs. In keeping with a recent DS meta-analysis (73), interferon response terms (fig. S4), as well as mitochondrial pathways and apoptotic terms (fig. S3), are particularly exacerbated in T21 neural cultures. Consistent with these results, we replicate impaired survival of T21 excitatory forebrain neurons reported previously (17, 31, 33, 54, 61, 62) and demonstrate increased cell death in T21 interneurons relative to isogenic euploid controls using the same methodology (Fig. 5). In addition, we observe reduced translation of EGFP (fig. S5). Because GSEA-enriched terms and related genes responded to *XIST*-mediated T21 dosage correction, they likely reflect cellular phenotypes that depend on ongoing excess chr21 expression and may therefore remain amenable to T21 dosage correction after completed development.

During early neural differentiation, we observe that T21 NPCs produce an excess of astrocytes at the expense of neurons (Fig. 6 and fig. S6), which is consistent with astrogliosis noted in fetal DS (31, 33, 35). Because *XIST*-mediated T21 silencing remains inducible during differentiation and persists into the NPC stage, neurogenesis is fully rescued when T21 dosage is corrected (Fig. 6), further indicating that T21 dosage correction is complete (Fig. 4 and fig. S2C). This is consistent with a prior report using T21-*XIST* dosage correction (30), but we can attribute this neurogenic rescue to suppression of a conserved T21 bias to advance astrogenesis, rather than slowed commitment of T21 NPCs (Fig. 6). We replicate this observation at the onset of cortical astrogenesis in Ts65Dn embryos (E18.5), which show a significant increase in S100B⁺ cells relative to wild-type embryos, while the density of Ki67⁺ neural progenitors remains unchanged (fig. S6). Several chr21 genes have been suggested to play a role in this astrogenic lineage bias, including amyloid precursor *APP*, *S100B*, and *DYRK1A* (33, 37). In addition, it is possible that cellular stress pathways affect NPC lineage decisions, as seen in rodent models of neurogenesis (74). One possible culprit may be oxidative stress that is elevated in DS iPSC-derived neurons and NPCs (43, 62) and also implicates these and additional chr21 genes (16, 33, 55).

We also examined T21-*XIST* iPSC-derived mature neural lineages after forcing NPCs to terminally differentiate, and thus commit to terminal neural cell fates via notch inhibitor DAPT (Fig. 7, A and B). This more mature (~9 to 12 weeks), postmitotic neural population is composed of terminally differentiated neurons and astrocytes, as well as residual neural progenitors and some oligodendroglial lineages (Fig. 8 and fig. S7). A large fraction of this terminal postmitotic

population can induce *XIST* and attract repressive H2AK119ub on chr21 in response to dox (Fig. 7, C and D), regardless of whether they were never exposed to dox before cessation of the DAPT treatment (pD) or were treated with only an LD (1% of the standard 1 μ M) dox concentration before DAPT treatment. In contrast, a previously reported T21-*XIST* system could not be induced at all anymore in postmitotic monolayer neural cultures (30).

Our results indicate that our T21-*XIST* system represents a major improvement, which we attribute to technical characteristics of transgene expression. First, our system uses a *UBC-rTTA* construct integrated at the AAVS “safe-harbor” locus, in contrast to prior studies that used *EF1 α* (24) or *CAG* promoters (30) at this locus or redelivered a high-copy *EF1 α -rTTA* construct via piggy-Bac to NPCs (75). Second, there may be sequence differences in these human *XIST* cDNA constructs that could affect the mature *XIST* RNA. Third, we integrated our *XIST* cDNA transgene outside of *DYRK1A*, not only to minimize its impact on *DYRK1A* before dox treatment but also to avoid attracting gene body-associated DNAm from overlapping transcription, which serves to suppress intragenic transcription start sites (76).

We assessed whether *XIST* induction in terminal, postmitotic neural cell types (pD) was as effective in correcting T21 dosage as it was during differentiation (d0) using three independent analytic approaches: chr21^P allele representation, normalized expression across chr21, and differential expression across the transcriptome (Fig. 8 and figs. S7 and S8). The chr21^P allele is effectively repressed to nearly the same degree in *XIST*⁺ pD as in d0 cells, especially in neurons (Fig. 8B and fig. S7). Likewise, both the median sum of normalized chr21 expression by cell and the entire distribution of cells shift toward the euploid mean ratio (Fig. 8 and fig. S7). The same significant shift is observed when aggregating the mean ratio across cells for individual genes (Fig. 8 and fig. S7). While some residual cycling NPCs retain excess expression in a subset of chr21 genes far [~20 Mbp (mega-base pairs)] from the *XIST* integration site (figs. S7 and S8), both normalized expression and allele-specific metrics indicate that *XIST* represses T21 dosage across all cell type groups, most effectively in postmitotic neurons. The transcriptome-wide analysis mirrors these results: Differential expression in *XIST*⁺ d0 and pD cells correlates significantly with that of euploid cells when compared to noninduced, *XIST*-negative T21 cells (Fig. 8 and fig. S8). Likewise, canonical pathways significantly enriched by GSEA in *XIST*⁺ d0 and pD cells match and follow the direction of change observed in the euploid to T21 comparison (Fig. 8 and fig. S8). In sum, these data demonstrate that postmitotic terminal neural cell types remain responsive to chr21 gene dosage. Enriched GSEA terms related to synaptic activity for neurons and calcium signaling for astrocytes, previously noted to be aberrant (77). This motivates several avenues for future investigation, for example, to dissect neuron-intrinsic and -extrinsic phenotypes that will be relevant for developing cell type-specific interventions (78) or to identify pathways that remain amenable to novel therapeutic approaches (14).

Regarding *XIST* biology, our results suggest that human neural lineages remain competent to initiate *XIST*-mediated heterochromatin deposition even in noncycling cells, provided *XIST* can be induced. Similar developmental plasticity in initiating (28, 29) or reinitiating (79, 80) *XIST*-mediated repression was previously reported only for proliferative hematopoietic cell lineages. Our work therefore suggests that *XIST* may be able to reestablish X chromosome

inactivation even outside of pluripotency and hematopoiesis, which is relevant to recently reported X chromosome conformational changes in the female brain across the estrous cycle (81).

In addition, prior reports of *XIST* induction in human HT1080 fibrosarcoma cells indicate that spreading of autosomal gene silencing remains reversible (82) and effective only near its site of integration (83). Both of these observations may be affected in part by *XIST* repression of haploinsufficient genes, which are not uncommon on mammalian autosomes, making whole or partial trisomy a valuable research tool to better understand the determinants of *XIST* spreading (84). In iPSCs, our T21-*XIST* system repressed virtually every chr21-linked gene without measurable impact of its linear distance from the *XIST* integration site, across a large span of expression values and in irreversible fashion (Fig. 2). The human inactive X in pluripotent stem cells frequently undergoes progressive reactivation following loss of *XIST* expression (85), the order of which we recently showed was determined in part by the distance to the nearest escapee gene (86). While our T21-*XIST* w/d was limited to 6 weeks, we found little evidence of reactivation over this period, indicating that DNAm served to maintain T21 silencing (Fig. 2). One exciting possibility to reconcile irreversible silencing of chr21 and contiguous reactivation of the inactive X (86) is that the latter may depend on the maintenance of active chromatin in escapee genes to seed reactivation when *XIST* expression is lost. Whether the epigenetic stability of the silenced chr21 is due to the lack of chr21 genes escaping *XIST* to seed any reactivation, or the levels of *XIST* before w/d, and to which degree these two aspects are related represents productive areas for future investigation.

MATERIALS AND METHODS

Experimental design

Reprogramming, iPSC validation, and culture

Human male fibroblast line (GM00260) mosaic for T21 was obtained from the Coriell Institute (Camden, NJ) and reprogrammed by the University of Connecticut's Cell and Genome Engineering Core using the CytoTune iPSC 2.0 Sendai Reprogramming Kit (Thermo Fisher Scientific, Waltham, MA). Genomic DNA from iPSC clones was screened via duplex TaqMan CN assay (*DYRK1A*, Hs01748441_cn and ribonuclease P, Thermo Fisher Scientific) to select euploid and T21 lines, followed by additional screening for chr17q TaqMan CN assay (*SEC14L1*, Hs05476397_cn), and the human pluripotent stem cells (hPSC) genetic analysis kit (STEMCELL Technologies, Vancouver, Canada). Interphase and M phase nuclei were also screened via fast-FISH (WiCell, Madison, WI) using chr20q (*BCL2L1*) and centromere enumeration probes for chr8, chr12, chr17, and chrX, alongside a SureFISH assay for chr21q (*DSCR8*). Selected iPSC lines were further screened by aCGH (Infinium BeadChip CytoSNP 850K assay, Illumina, San Diego, CA) at the Center for Genome Innovation, Institute for Systems Genomics at the University of Connecticut.

T21 and euploid iPSCs were cultured on mitotically inactive mouse embryonic fibroblasts (MEFs) in standard iPSC medium in 5% CO₂ at 37°C [80% Dulbecco's modified Eagle's medium/F12 (DMEM/F12), 20% knockout serum replacement, 1% GlutaMAX, 1% nonessential amino acids, 0.1% β -mercaptoethanol, and basic fibroblast growth factor (8 ng/ml); Thermo Fisher Scientific] and passaged weekly by manual disruption of 6 to 10 representative colonies. For iPSC cultures requiring dox induction, 2 μ M dox was added to the culture medium.

Plasmid construction

For PCR amplifications, either Herculase II polymerase (Agilent, Santa Clara, CA), Platinum Taq High Fidelity (Thermo Fisher Scientific), Advantage 2 Polymerase (TaKaRa Bio, Shiga, Japan), or Q5 Hi-Fidelity DNA Polymerase (New England Biolabs) was used. For cloning reactions except the large *XIST* insert steps, ligations were performed with T4 DNA ligase (2,000,000 U/ml; New England Biolabs), and DH10B homemade chemically competent cells were used at 37°C. For all cloning with *XIST* cDNA fragments aside from ligation of oligo not directly followed by transformation (which used the same T4 DNA ligase), the TaKaRa DNA Ligation Kit LONG (TaKaRa Bio) was used along with NEB Stable Competent *Escherichia coli* (New England Biolabs) with bacterial incubations at 25° to 30°C to mitigate instability in initial steps observed at 37°C.

To clone the *XIST* transgene cDNA in a temporary pUC19 vector, a 10-kb fragment containing most of *XIST* exon 1 was cut from a fosmid (WI2-935P22, BACPAC Genomics) with Sac II and Psh AI. Linker oligos were used to clone the 10-kb Sac II and Psh AI fragments into the Kpn I and Xba I sites of pUC19, respectively. The 5'-most end of *XIST* exon 1 was PCR-amplified, concurrently adding a 5' Pme I restriction site. The resulting PCR product was digested with Pme I and Btg ZI and cloned in between the Pme I/Btg ZI restriction sites of the *XIST* exon 1-containing plasmid. The 3' end of exon 1 through exon 6 was amplified from cDNA of Wi-38 cells (AG07217, Coriell Institute), while adding a 3' Sal I restriction site. The resulting PCR was digested with Psh AI and Sal I and cloned between the Psh AI and Sal I sites of the plasmid from the prior step to complete the *XIST* cDNA construct. The UBC promoter from the FUGW construct (Addgene, plasmid #14883) (87) was cloned into AAVS1-Neo-M2rtTA (Addgene, plasmid #60843) (88). The UBC promoter was PCR-amplified with flanking Pvu II and Fse I sites and cloned into the Ale I and Fse I sites on the AAVS1-neo-M2rtTA plasmid. This rtTA-advanced open reading frame was replaced with rtTA3G from the pCMV-Tet-3G plasmid (TaKaRa Bio) by Xba I and Xma I digestion and cloning of three separate fragments to create the final rtTA vector AAVS1-NEO-UBrtTA-3G.

To generate the final targeting vector, pTRE3G (TaKaRa Bio) was used as the backbone, following excision of an Xba I fragment to reduce the size of the vector via removal of the SV40 small intron, nuclear localization signal (NLS), and SV40 polyadenylation [poly(A)] sequences. The 5' homology arm for chr21 was generated by PCR with Eco RI sites on each primer using the genomic DNA of the destination cell line as the template. This PCR product was ligated into the Eco RI sites of the pTRE3G vector to make pTRE3G-5P. Next, a fusion PCR product was generated, harboring a bovine growth hormone (BGH) poly(A) site amplified from p452 (89) and the 3' homology arm using overlapping PCR from the genomic DNA of the destination cell line. This PCR product was cloned into the Pst I and Bam HI sites of the pTRE3G-5P to make pTRE3G-5P3P. Next, a loxP-flanked PGK-puro-TK fragment was removed from vector p452-puroTK by Xho I digest. The fragment was cloned into the Xho I sites of the vector pTRE3G-5P3P. This p452-puroTK vector was derived from plasmids p452 and plasmid pLCA.66/2272 (Addgene, plasmid #22733) (90) by removing the PGK-puroTK cassette with Age I and Bbs I and cloning that fragment into p452 using the same enzymes. To add the *XIST* cDNA construct, this CMV-puroTK-TRE3G vector was digested with Mlu I and Sbf I, and a phosphorylated linker oligo was ligated to purified, digested backbone, creating a Sac I-compatible overhang. Following purification,

this vector was ligated to the Sbf I-Sac I fragment containing the *XIST* cDNA construct to create the TRE3G-*XIST* cDNA targeting vector. Homology arms amplification primers were as follows: 5' arm, aatagaattcGCCTGGTTGACAGAGTGAGATCG and aatagaattcTCAATCCAGGTGTATAGAGTGTGAGT; 3' arm, aatagatccTCCCTCCGAAAACAACAAACGGA and gggatgcggtggctctatggTTGGTTCACAGCCAATTTTCAGGCTCACCGTGTCTTCAGACA.

Human iPSC targeting and screening

Targeting was performed using a Lonza 4D-Nucleofector (Lonza, Basel, Switzerland) with primary cell kit P3 and program CD-150. AAVS1-Neo-UBC-rtTA was targeted to chr21 of the T21 cell line 198-5. Two micrograms of each AAVS1-targeting TALEN (91) was nucleofected along with 6 µg of AAVS1 integration vector. Cells were plated on mitotically inactivated DR4 MEFs (American Type Culture Collection, Manassas, Virginia) after nucleofection. After 96 hours, cells were cultured with G418 at a concentration of 25 µg/ml. Selection was done for a total of 6 days. Resulting colonies were isolated and screened for targeting. cDNAs from targeted clones were tested for expression of rtTA by reverse transcription (RT)-qPCR. AAVS1 TALEN-L (Addgene, plasmid #59025) and AAVS1 TALEN-R (Addgene, plasmid #59026) (92) were used for targeting the UBC-rtTA3G Integrants were screened using (AAVS1_scr_F/Neo_R and AAVS1_3'scr_R/rtTA_F). Integrants for UBC-rtTA3G were screened with AAVS1_scr_F, Neo_R and AAVS_3'scr_R, and rTTA_F sequences were as follows: AAVS1 scr forward, TGAGCTCTACTGGCTTCTGCNeo reverse, CGTGCAATCCATCTTGTTCA; AAVS1 3'scr reverse, GGTCCAGGCCAAGTAGGT; rTTA forward, ATGCTCCCCGGGTAACCTAAG.

For targeting *XIST* transgene via CRISPR, a guide designed to target the minor allele of rs2835797 (starred), creating a protospacer adjacent motif site (ATCTTTGCTCAGTTCGATTGTGG*) on the chr21^P copy without cutting the chr21^{M/M2} alleles, was cloned into PX459V2 (Addgene, plasmid #48139) (93) at the Bbs I site by annealing and ligating overlapping oligos. Two micrograms each of this CRISPR guide plasmid was used along with 6 µg of *XIST* cDNA-targeting vector. Cells were plated on DR4 MEFs, and after 96 hours, puromycin was added to the culture at a concentration of 0.5 µg/ml for a total of 4 days. Resulting colonies were isolated and genotyped for targeting by PCR, followed by verification of clones by sequencing across the target to confirm the loss of the targeted allele; sequences were as follows: CH21 xist scr F1, AGGTGGGAGAATTGAACACG; CH21 xist scr F2, GAGCTGAGATTGCACCACCTG; CH21 internal R1, GCCAGAGGCCACTTGTGTAG; CH21 internal R2, CTAAAGCGCATGCTCCAGAC; *XIST* internal F1, TGAGCCACAATTGGTTTTGA; *XIST* internal F2, AAGTTTCTG-GCGTCGACCT; *XIST* SCR R1, TCTCATAAACCGCCTTCCTG; *XIST* SCR R2, GGCGTGTCAAGTGAGAATGT; CH21 xist C1 PCR F, CTGTGTGCTCTGTCTGGAT; CH21 xist C1 R, TGTCTGAAGACACGGTGAGC; CH21 xist C1 seqF, GCTTCTTGC-CACCTACTTGC.

Nucleic acid purification

Genomic DNA was purified from fresh or frozen pelleted cells using three different methods depending on application. For colony PCR screening, genomic DNA was extracted via standard high-salt chloroform extraction. For standard PCR and array hybridization, cell pellets were resuspended in either cell lysis buffer 1 [10 mM tris-HCl (pH 8.0), 100 mM NaCl, 10 mM EDTA (pH 8.0), 1% SDS, and proteinase K (200 µg/ml)] or cell lysis buffer 2 [10 mM tris-HCl (pH 8.0),

200 mM NaCl, 10 mM EDTA (pH 8.0), 0.5% sarcosyl, and proteinase K (1 mg/ml)] and incubated at 55°C for 3 hours to overnight with optional ribonuclease A treatment (10 µg/ml) following at 37°C for 5 min. Genomic DNA was isolated using phenol:chloroform:isoamyl alcohol (25:24:1, v/v) (Invitrogen, Waltham, MA), precipitated with either isopropanol or 300 mM sodium acetate with 2 volumes of 100% chilled ethanol and 15 min at –80°C, washed with 70% ethanol, and resuspended in TE buffer. For linked-read WGS, high-molecular weight (HMW) genomic DNA was prepared from fresh or frozen iPSC cell pellets, following the protocol listed in the Chromium Genome Reagent Kits v2 User Guide (10x Genomics, Pleasanton, CA), using the MagAttract HMW Kit (QIAGEN, Germantown, MD) with minor modifications. Plasmid and fosmid DNA were purified with either the Zippy Plasmid Miniprep Kit or ZymoPURE II Plasmid Midiprep Kit (Zymo Research, Irvine, CA). Following restriction digests or PCR, DNA purification was performed with the Monarch PCR & DNA Cleanup Kit (New England Biolabs, Ipswich, MA) or the DNA Clean & Concentrator Kit (Zymo Research). For RNA isolation, the PureLink RNA Mini Kit (Invitrogen, Carlsbad, CA) was used, followed by cDNA synthesis using the iScript gDNA Clear cDNA Synthesis Kit (Bio-Rad Laboratories, Hercules, CA).

Real-time quantitative polymerase chain reaction

Gene expression was measured via quantitative real-time PCR using the iTaq Universal SYBR Green Supermix (Bio-Rad Laboratories) and the ΔC_T method. Primer specificity was confirmed by melting curve analysis, and relative expression was calculated as % *GAPDH* ($100/2^{\Delta C_T}$). TaqMan CN assays were normalized to 198-1 genomic DNA. HOT FIREPol Probe Universal PCR Mix Plus–no ROX (Solis BioDyne, Tartu, Estonia) was used as per the manufacturer's instructions, using 4 ng of high-quality genomic DNA template in 20 µl of reactions. The hPSC Genetic Analysis Kit (STEMCELL Technologies) was used following the manufacturer's instructions. All qPCR reactions were performed in triplicate in a Bio-Rad CFX 96 real-time system.

Cytogenomics, DNAME, linked-read WGS, and mRNA-seq

For cytogenomic analysis, genomic DNA was labeled and hybridized to the Infinium BeadChip CytoSNP 850K array (Illumina, San Diego, CA) according to the manufacturer's protocols. For DNAME analysis, genomic DNA was bisulfite-converted using the EZ DNA Methylation Kit (Zymo Research, Irvine, CA), then labeled, and hybridized using the Infinium Methylation EPIC BeadChip Kit (Illumina) following standard protocol of each manufacturer. Both types of arrays were scanned on a NextSeq 550 system (Illumina). HMW genomic DNA was sequenced to ~30× coverage on a HiSeq X (Illumina), following library preparation on the 10x Genomics linked-read platform at the Center for Genome Innovation, Institute for Systems Genomics at the University of Connecticut. For standard mRNA-seq, libraries were prepared using the Illumina stranded mRNA kit, and 100-bp paired-ends reads were sequenced to an average depth of 40 million reads per replicate on the NovaSeq 6000 (Illumina, San Diego, CA).

IF and XIST RNA FISH

For XIST RNA FISH, cells were permeabilized with 0.5% Triton X-100 and 2 mM ribonucleoside vanadyl complex in CSK buffer [10 mM Pipes (pH 6.8), 100 mM NaCl, 3 mM MgCl₂, and 300 mM sucrose], fixed in 4% paraformaldehyde (PFA) in phosphate-buffered saline (PBS), and then dehydrated through a series of ethanol washes (70, 80, 90, and 100%). Digoxigenin-labeled XIST probe hybridization

was performed overnight in a humidity chamber at 42°C. Anti-digoxigenin antibody (Thermo Fisher Scientific, 700772) was hybridized for 1 hour at room temperature. Secondary antibody hybridization (Alexa Fluor; Invitrogen; 1:500) was followed for 1 hour at room temperature. Nuclear DNA was counterstained with Hoechst 33342 dye. Slides were imaged with an EVOS FL Auto2 system (Thermo Fisher Scientific).

For IF, cells were grown in Nunc Lab-Tek II glass chamberslides coated with poly-D-lysine (PDL) and laminin (for neural differentiation) or permanox chamberslides with MEFs (iPSCs). Cells were fixed in 4% PFA (Electron Microscopy Sciences, Hatfield, PA) for 10 min at room temperature, rinsed three times with PBS for 5 min, and then permeabilized in 1% Triton X-100 in PBS for another 10 min. Samples were blocked in blocking buffer containing PBS, 0.1% Triton X-100, 5% bovine serum albumin, and 2% normal goat serum (MilliporeSigma). Cells were placed in antibodies diluted in blocking buffer overnight at 4°C in a humidity chamber. Primary antibodies were used as follows: MAP2 (Abcam, ab5392; 1:10,000), S100B (Sigma-Aldrich, s2532; 1:1000), H2AK119ub (Cell Signaling Technology, 8240; 1:1600). Following three washes in 0.1% Triton X-100 in PBS for 5 min, cells were labeled with Alexa Fluor secondary antibodies at 1:500 for 1 hour at room temperature. Nuclei were counterstained with Hoechst 33342, and slides were preserved in ProLong Gold Antifade Mountant (Thermo Fisher Scientific).

Neural differentiation

T21 and euploid iPSCs were passaged manually onto MEFs and in iPSC medium. On day 2 after passage, cultures were switched into N2B27 neural differentiation medium (NDM) [neurobasal medium (Gibco), 2% B27 (Gibco), 1% N2 (Gibco), DMEM/F12, insulin (25 µg/ml; Sigma-Aldrich), holo-transferrin (100 µg/ml), 100 µM putrescine, 20 nM progesterone, and 30 nM selenite, 1% ITS-A (Gibco), 1% penicillin-streptomycin (Gibco), and 1% GlutaMAX (Gibco), supplemented with Noggin at 500 ng/ml (R&D Systems)], as described in (57). Cultures were fed and supplemented with Noggin every other day through day 10. For neural differentiation with dox induction, 1 µM dox, or 0.01 µM for low-dose cultures, was added to the culture medium. Cultures were fed N2B27 until the appearance of mature rosette structures (d14 to d16). Rosette-stage cultures were passaged manually 1:1 onto PDL and laminin-coated tissue culture plates and grown to confluence. Cells were cultured until d23 and passaged enzymatically with Accutase (Invitrogen) onto PDL and laminin-coated substrates at 1.9×10^4 to 2.2×10^4 cells/cm². At d25, cultures were switched to NDM [neurobasal medium (Gibco), 2% B27 (Gibco), 1% nonessential amino acids (Gibco), 1% penicillin-streptomycin (Gibco), 2 mM GlutaMAX (Gibco), brain-derived neurotrophic factor (BDNF; 10 ng/ml; Peprotech), glial-derived neurotrophic factor (10 ng/ml; Peprotech), 1 µM cyclic adenosine 5'-monophosphate (Sigma-Aldrich), and 200 µM ascorbic acid (Sigma-Aldrich)]. Cells were cultured in NDM until assay end point. For DAPT-treated cultures, DAPT (Tocris Bioscience) was added for 5 days at 10 µM. For EdU labeling, EdU was added at 5 µM for 24 hours and detected using the Click-iT EdU Imaging Kit (Invitrogen). Dox (1 µM) was added to EdU-labeled pD cultures at the time of EdU addition/labeling.

For longitudinal imaging of forebrain cortical neurons and interneurons, euploid (198-1) and T21 (198-5) iPSCs were maintained on Matrigel-coated plates in mTESR medium (STEMCELL Technologies) before differentiation. Forebrain cortical neurons were derived from iPSCs as described in (65). Briefly, neural differentiation was

induced with Smad inhibitors dorsomorphin (1.5 μ M) and SB431542 (10 μ M) for 11 days. Inhibitors were removed on day 12 and supplemented with retinoic acid (0.05 μ M) on day 16. At day 20, cells were dissociated with 0.05% trypsin-EDTA, resuspended in medium with BDNF (2 ng/ml), glial-derived neurotrophic factor (2 ng/ml), and retinoic acid (0.05 μ M), and plated 1:2 onto poly-L-ornithine-laminin-coated dish. For interneuron differentiation, iPSCs were first dissociated as colonies with collagenase IV/dispase (1 mg/ml each; Invitrogen) and further into single cells using 0.05% trypsin-EDTA. Then, 10,000 cells were plated on low-attachment round-bottom 96-well plate to form suspension embryoid bodies in optimized B27 + five factor medium, as described in (94). On day 7, suspension embryoid bodies (35 to 40 per well) were transferred to six-well Matrigel-coated plates, without Y-27632. On day 14, medium was replaced with the addition of purmorphamine (1 μ M) only. On day 25, adherent embryoid bodies were dissociated using 0.05% trypsin-EDTA, passed through 70- μ m cell strainer, and plated at a density of 10,000 to 25,000 cells/cm² onto poly-L-ornithine-laminin-coated plates. Neurons were matured in B27 medium containing DAPT (10 μ M) and BDNF (2 ng/ml). The pHR-hSyn1-RGEDI-P2a-EGFP lentivirus (multiplicity of infection = 1) was added to forebrain cortical neurons (day 35) and interneurons (day 56) for survival analysis as described (58) and imaged with robotic microscopy (95) every 12 hours for 10 days. The cells were maintained in an environmental chamber with 5% CO₂ during imaging. These live cell images were taken on an inverted microscope (Nikon Ti-E) at \times 20 magnification. A customized software controlling Micromanager (version 2.0 gamma) is used to allow the automated runs return to the same field of view on the plate for longitudinal imaging in three-dimensional space.

Single-nucleus RNA sequencing

Neural cultures were treated with TrypLE (Life Technologies) for 4 min at 37°C, and cells were counted with Trypan blue on the Countess Automated Cell Counter. Nucleus isolation was performed with the Nuclei Isolation Kit: Nuclei EZ Prep (Sigma-Aldrich) with some modifications. Briefly, cells were centrifuged at 1330 rpm for 3.5 min, medium-aspirated, and resuspended in Nuclei PURE Lysis Buffer containing 1 M dithiothreitol, 10% Triton X-100, and RNasin. Nuclei were centrifuged at 500g and 4°C for 5 min in a swing-bucket rotor centrifuge, and lysis buffer was aspirated. Nuclei resuspended in Nuclei PURE Sucrose Cushion buffer, and RNasin was pelleted at 500g and 4°C for 5 min, resuspended again in 25% iodixanol solution (0.28 ml of Nuclei PURE Sucrose Cushion buffer containing RNasin + 0.2 ml of 60% iodixanol), and underlayered by corresponding 30 and 35% iodixanol solutions. Nuclei traverse the 25% and 30% layers of this density gradient upon centrifugation (3166g at 4°C for 30 min) and were collected from the 30 to 35% interface in a volume of 0.3 ml. Resuspended in PURE Storage Buffer (1 ml) and 5 μ l of RNasin, nuclei were pelleted at 3166g for 15 min at 4°C, resuspended in remaining 0.1 ml, and counted again. Isolated nuclei were stored at -80°C until fixation. Nucleus fixation was performed according to the Evercode Fixation v2 protocol (Parse Biosciences). Nuclei were counted after fixation and barcoded using the Evercode WT mini v2, following the manufacturer's instructions. Sublibraries were quantified using the Agilent Tapestation, pooled in proportion to their respective nuclei counts, and sequenced on MiSeq v2 and NextSeq 550 v2.5 mid-output kits (Illumina).

Animals

Ts65Dn (strain #005252) mice were obtained through crossings of a B6EiC3Sn a/A-Ts65Dn female to F1 hybrid B6C3F1/J males purchased from the Jackson Laboratory. Genotyping was performed by amplifying genomic DNA with an in-house protocol. The colony of Ts65Dn mice was maintained in the Animal Facilities in the Barcelona Biomedical Research Park (PRBB; Barcelona, Spain). Mice received chow and water ad libitum under controlled laboratory conditions with temperature maintained at $22^{\circ} \pm 1^{\circ}\text{C}$ and humidity at $55 \pm 10\%$ on a 12-hour light/dark cycle (lights off at 20:00). The control group consisted of wild-type euploid littermates. All experimental procedures were approved by the local ethical committee (Comité Ético de Experimentación Animal del PRBB; procedure number MDS-12-1464P3) and met the guidelines of the local (law 32/2007) and European regulations (EU directive no. 86/609, EU decree 2001-486) and the Standards for the use of Laboratory Animals no. A5388-01 [National Institutes of Health (NIH)].

Slide immunohistochemistry

Breeding pairs were established so that vaginal plugs could be checked twice daily. The presence of a vaginal plug was designated as E0.5. A 10% weight gain at E10 was used to confirm pregnancy. Male and female embryos were collected from pregnant trisomic dams at E18.5, chilled, decapitated immediately, and processed for fluorescent immunohistochemical staining. Fetal heads were immersed in 4% PFA (Sigma-Aldrich), and the brain was dissected 24 hours later and immersed again in PFA overnight. Brains were cryoprotected by immersion in 30% sucrose solution and embedded in optimal cutting temperature compound for posterior histological processing. Embryo heads were embedded in optimal cutting temperature compound, and embedded tissue was frozen rapidly and either stored at -80°C or immediately sectioned into 20- μ m-thick frozen sections using a cryostat (Leica, CM3050S). Histological sections were placed in Superfrost slides and placed at -20°C . We processed two sections at three different coordinates ($+1.81/2.52/3.15$ from Bregma). Slices were fixed with methanol and incubated with blocking buffer [tris-buffered saline (TBS) with 0.5% Triton X-100 and 6% normal donkey serum]. Primary antibodies were diluted in TBS++ (TBS with 0.1% Triton X-100 and 6% normal donkey serum): anti-S100B (rabbit, Synaptic Systems, #287003; 1:1000) and anti-Ki67 (rabbit, Abcam, ab15580; 1:500). Slices were incubated with primary antibodies overnight. After three washes with TBS, sections were incubated with the following secondary antibodies diluted in TBS++: goat anti-rabbit (Alexa Fluor 594, Invitrogen, A11012; 1:500) and goat anti-rabbit (Alexa Fluor 488, A-11008; 1:500). Slices were washed three times with TBS and incubated for 10 min with Hoechst 33342. Last, sections were mounted on glass slides using an aqueous mounting medium, Mowiol. To quantify the density of S100B cells, six sections per animal were imaged using a Leica TCS SP5 inverted scanning laser microscope (Leica Microsystems). Fifteen- to 16- μ m thick z-stacks (512 by 512 resolution, 8 bits) of each region of interest in the cortex of embryos were acquired using a 20 \times objective (numerical aperture = 0.8).

Statistical analysis

Image analysis

For IF (H3K27me3 and H2AK119ub) and *XIST* FISH in iPSCs, automated image quantification relative to all Hoechst 33342-labeled cells was performed using a custom CellProfiler pipeline (96), which was run in two phases. First, images were optimized for

computer recognition using the following CellProfiler functions on each channel of each image: RescaleIntensity, CorrectIlluminationCalculate, CorrectIlluminationApply, and ReduceNoise. Then, signals for nuclei, IF, and *XIST* FISH were quantified using the IdentifyPrimaryObjects functions, and counts for IF or *XIST*-positive nuclei were obtained using RelateObjects and FilterObjects. Images were output alongside outline annotations for objects recognized by CellProfiler to visually verify accuracy and consistency of automated counts. For EdU and *XIST* FISH, as well as IF of iPSC-derived neural lineages (MAP2 and S100B), images were imported, and labeled cells were counted manually using ImageJ (NIH, Bethesda). Differences in median fraction of labeled cells were assessed by two-tailed Wilcoxon rank sum test.

For longitudinal imaging of forebrain cortical neurons and interneurons, images were segmented using EGFP morphology, background-subtracted, aligned together across time points, and then extracted channel intensity and feature information from each neuron into a csv file. Survival analysis was performed by defining the time of death as the point at which the GEDI ratio (RGEDI signal:EGFP expression) of a longitudinally imaged neuron exceeds the empirically calculated GEDI threshold (58). In addition, single cells were tracked (59), and cumulative death was calculated using linear mixed model with Holm correction in R studio (version 4.0.4).

For slice immunochemistry images, labeled cells were manually counted using ImageJ (NIH, Bethesda). Cell counting was performed using the Cell Counter plugin on ImageJ in a maximum projection of all z-stacks (1- μ m step size). Cell counts from the cortex were processed first by image, then by coordinate (two images were taken from each coordinate), then by animal, and lastly by genotype. To quantify the density of Ki67 cells, three sections per animal were imaged in the same form as S100B but imaged the ventricular zone of the cortex, the area with higher proliferation. An area of 100 μ m² was delimited to normalize across sections and because of the high density of cells in this area. Outliers in datasets from both euploid and trisomic mice were statistically determined using a calculation of interquartile range. All data points outside of the interquartile range fences were excluded from analysis without bias. All variables were assessed with a two-tailed, independent samples Student's *t* test and passed both the Shapiro-Wilks normality test and an equal variance test.

Expression and DNAME analysis

FASTQ files were quality controlled using FASTQC, reads were filtered, and adapter-trimmed using BBDuk (97). Expression quantification was performed using Salmon (98), and differential expression analysis was performed using DESeq2 (99). Gene set enrichments were performed using the GSEA function from the R package clusterProfiler (100) on the following gene sets: Biocarta, Gene Ontology (Biological Processes, Cellular Components, and Molecular Functions), Kyoto Encyclopedia of Genes and Genomes, Pathway Interaction Database, Reactome, and WikiPathways. For DNAME analysis, the MethylePIC IDAT files were processed using the R package minfi and its preprocessIllumina function to obtain methylation β values (101). Promoter probes were defined as having one of the following designations in the array manifest file: TSS1500, TSS200, or 5'_UTR. For comparing to previously described T21-*XIST* system (fig. S2B), we downloaded raw counts and used DESeq2 to calculate VST counts for all D21, T21, T21-*XIST* -dox, and T21-*XIST* +dox samples. To calculate the distribution of VST differences from each respective T21 condition in fig. S2B, we only used

the 150 chr21 genes that were expressed in both datasets herein and in common with a third dataset from (30). We used VST counts rather than differential expression FCs to mitigate differences in experimental design between our study and the prior report that could otherwise affect DESeq2 log₂FC and *P* values.

Phased allelic RNA-seq analysis

The 10x Genomics Long Ranger pipeline was used to align reads, call and phase SNPs, indels, and structural variants from linked-read WGS reads. The processed FASTQs from above were aligned using HISAT2 to the hg38 human reference genome (102). Relevant chr21 SNPs were extracted from the Long Ranger output and used to obtain haplotype gene expression counts from aligned RNA-seq bam files using the Phaser software package (103). While this provided reliable intragenic phasing, for intergenic phasing on chr21, we relied on the imbalanced haplotype gene expression in the T21, compared to its isogenic euploid controls. The higher T21 over D21 represented haplotype was designated as the major (duplicated or chr21^{M/M2}) haplotype and the other as the minor haplotype (chr21^P).

Single-nucleus RNA-seq analysis

FASTQ files were processed using the split-pipe pipeline (Parse Biosciences) and imported to Seurat (104), yielding 78,478 reads per cell on average. We excluded nuclei with over 10% reads mapping to the mitochondrial genome, fewer than 2500 mapped reads, fewer than 1500 genes detected, or over 7500 genes detected, removing altogether 167 of 2285 nuclei. On average, 3568 genes and 11,171 transcripts were detected in nuclei passing this filter. Following normalization and cell cycle scoring, the data were SC-transformed (71) while regressing out the mitochondrial read fraction, and samples were integrated. Uniform Manifold Approximation and Projections (UMAPs) were generated using the first 30 principal components, and clusters were labeled under default settings. Cell types were identified and grouped using markers from (67) and scType (68). Allelic counts from single nuclei were phased as described above and aggregated across all chr21 genes to mitigate the impact of transcriptional bursts. Chr21 dosage by cell (aggregating across chr21 genes) or by gene (aggregating across cells) was performed on counts-per-million normalized expression. Differences in median chr21 allele representation or chr21 dosage ratio were assessed by two-tailed Wilcoxon rank sum test and differences in distribution by two-sample Kolmogorov-Smirnov test. For differential expression analysis, Seurat functions PrepSCTFindMarkers and FindMarkers using the ROC (receiver operating characteristic curve) test were applied to compare euploid, *XIST*⁺ d0 and pD cells to *XIST*-negative T21 cells by cell type group. GSEA was performed as for bulk RNA-seq while limiting gene terms to Hallmark and canonical pathways (Kyoto Encyclopedia of Genes and Genomes, Reactome, WikiPathways, PID, and Biocarta) of MSigDB.

Supplementary Materials

This PDF file includes:

Figs. S1 to S8

Legends for data S1 to S4

Other Supplementary Material for this manuscript includes the following:

Data S1 to S4

REFERENCES AND NOTES

- G. T. Capone, B. Chicoine, P. Bulova, M. Stephens, S. Hart, B. Crissman, A. Videlefsky, K. Myers, N. Roizen, A. Esbensen, M. Peterson, S. Santoro, J. Woodward, B. Martin,

- D. Smith, Co-occurring medical conditions in adults with Down syndrome: A systematic review toward the development of health care guidelines. *Am. J. Med. Genet. A* **176**, 116–133 (2018).
2. S. E. Antonarakis, B. G. Skotko, M. S. Rafii, A. Strydom, S. E. Pape, D. W. Bianchi, S. L. Sherman, R. H. Reeves, Down syndrome. *Nat. Rev. Dis. Prim.* **6**, 9 (2020).
 3. Y. Kazuki, F. J. Gao, Y. Li, A. J. Moyer, B. Devenney, K. Hiramatsu, S. Miyagawa-Tomita, S. Abe, K. Kazuki, N. Kajitani, M. Uno, S. Takehara, M. Takiguchi, M. Yamakawa, A. Hasegawa, R. Shimizu, S. Matsukura, N. Noda, N. Ogonuki, K. Inoue, S. Matoba, A. Ogura, L. D. Florea, A. Savonenko, M. Xiao, D. Wu, D. A. S. Batista, J. Yang, Z. Qiu, N. Singh, J. T. Richtsmeier, T. Takeuchi, M. Oshimura, R. H. Reeves, A non-mosaic transchromosomal mouse model of down syndrome carrying the long arm of human chromosome 21. *eLife* **9**, e56223 (2020).
 4. Y. Kazuki, F. J. Gao, M. Yamakawa, M. Hirabayashi, K. Kazuki, N. Kajitani, S. Miyagawa-Tomita, S. Abe, M. Sanbo, H. Hara, H. Kuniishi, S. Ichisaka, Y. Hata, M. Koshima, H. Takayama, S. Takekura, Y. Nakahara, M. Hiratsuka, Y. Iida, S. Matsukura, N. Noda, Y. Li, A. J. Moyer, B. Cheng, N. Singh, J. T. Richtsmeier, M. Oshimura, R. H. Reeves, A transchromosomal rat model with human chromosome 21 shows robust Down syndrome features. *Am. J. Hum. Genet.* **109**, 328–344 (2022).
 5. Y. Herault, J. M. Delabar, E. M. C. Fisher, V. L. J. Tybulewicz, E. Yu, V. Brault, Rodent models in Down syndrome research: Impact and future opportunities. *Dis. Model. Mech.* **10**, 1165–1186 (2017).
 6. A. Bhattacharyya, Advancing knowledge of down syndrome brain development and function with human stem cells. *Am. J. Intellect. Dev. Disabil.* **25**, 90–92 (2020).
 7. I. K. Suzuki, P. Vanderhaeghen, Is this a brain which i see before me? Modeling human neural development with pluripotent stem cells. *Development* **142**, 3138–3150 (2015).
 8. J. van den Amele, L. Tiberi, P. Vanderhaeghen, I. Espuny-Camacho, Thinking out of the dish: What to learn about cortical development using pluripotent stem cells. *Trends Neurosci.* **37**, 334–342 (2014).
 9. M. R. Cookson, Evolution of neurodegeneration. *Curr. Biol.* **22**, R753–R761 (2012).
 10. K. Shabani, B. A. Hassan, The brain on time: Links between development and neurodegeneration. *Development* **150**, dev200397 (2023).
 11. X. Altafaj, E. D. Martin, J. Ortiz-Abalia, A. Valderrama, C. Lao-Peregrin, M. Dierssen, C. Fillat, Normalization of Dyrk1A expression by AAV2/1-shDyrk1A attenuates hippocampal-dependent defects in the Ts65Dn mouse model of Down syndrome. *Neurobiol. Dis.* **52**, 117–127 (2013).
 12. F. K. Wiseman, T. Al-Janabi, J. Hardy, A. Karmiloff-Smith, D. Nizetic, V. L. J. Tybulewicz, E. M. C. Fisher, A. Strydom, A genetic cause of Alzheimer disease: Mechanistic insights from Down syndrome. *Nat. Rev. Neurosci.* **16**, 564–574 (2015).
 13. S. Rosi, E. S. Frias, The integrated stress response: A central memory switch in down syndrome. *Cell Metab.* **31**, 15–17 (2020).
 14. P. J. Zhu, S. Khatiwada, Y. Cui, L. C. Reineke, S. W. Dooling, J. J. Kim, W. Li, P. Walter, M. Costa-Mattoli, Activation of the ISR mediates the behavioral and neurophysiological abnormalities in Down syndrome. *Science* **366**, 843–849 (2019).
 15. A. Tramutola, C. Lanzillotta, A. Arena, E. Barone, M. Perluigi, F. Di Domenico, Increased mammalian target of rapamycin signaling contributes to the accumulation of protein oxidative damage in a mouse model of Down's syndrome. *Neurodegener. Dis.* **16**, 62–68 (2016).
 16. E. Zamponi, N. Zamponi, P. Coskun, G. Quassollo, A. Lorenzo, S. A. Cannas, G. Pigino, D. R. Chialvo, K. Gardiner, J. Busciglio, P. Helguera, Nrf2 stabilization prevents critical oxidative damage in Down syndrome cells. *Aging Cell* **17**, e12812 (2018).
 17. P. Helguera, A. Pelsman, G. Pigino, E. Wolvetang, E. Head, J. Busciglio, ets-2 promotes the activation of a mitochondrial death pathway in Down's syndrome neurons. *J. Neurosci.* **25**, 2295–2303 (2005).
 18. P. Helguera, J. Seiglie, J. Rodriguez, M. Hanna, G. Helguera, J. Busciglio, Adaptive downregulation of mitochondrial function in down syndrome. *Cell Metab.* **17**, 132–140 (2013).
 19. F. Di Domenico, R. Coccia, A. Cociolo, M. P. Murphy, G. Cenini, E. Head, D. A. Butterfield, A. Giorgi, M. E. Schinina, C. Mancuso, C. Cini, M. Perluigi, Impairment of proteostasis network in Down syndrome prior to the development of Alzheimer's disease neuropathology: Redox proteomics analysis of human brain. *Biochim. Biophys. Acta Mol. Basis Dis.* **1832**, 1249–1259 (2013).
 20. S. Hwang, P. Cavaliere, R. Li, L. J. Zhu, N. Dephore, E. M. Torres, Consequences of aneuploidy in human fibroblasts with trisomy 21. *Proc. Natl. Acad. Sci. U.S.A.* **118**, e2014723118 (2021).
 21. M. M. Nielsen, C. Trolle, S. Vang, H. Hornshøj, A. Skakkebaek, J. Hedegaard, I. Nordentoft, J. S. Pedersen, C. H. Gravholt, Epigenetic and transcriptomic consequences of excess X-chromosome material in 47,XXX syndrome—A comparison with Turner syndrome and 46,XX females. *Am. J. Med. Genet. Part C Semin. Med. Genet.* **184**, 279–293 (2020).
 22. A. K. S. Roman, A. K. Godfrey, H. Skaletsky, D. W. Bellott, A. F. Groff, H. L. Harris, L. V. Blanton, J. F. Hughes, L. Brown, S. Phou, A. Buscetta, P. Kruszka, N. Banks, A. Dutra, E. Pak, P. C. Lasutschinkow, K. Keen, S. M. Davis, N. R. Tartaglia, C. Samango-Sprouse, M. Muenke, D. C. Page, The human inactive X chromosome modulates expression of the active X chromosome. *Cell Genomics* **3**, 100259 (2023).
 23. N. Tartaglia, S. Howell, S. Davis, K. Kowal, T. Tanda, M. Brown, C. Boada, A. Alston, L. Crawford, T. Thompson, S. van Rijn, R. Wilson, J. Janusz, J. Ross, Early neurodevelopmental and medical profile in children with sex chromosome trisomies: Background for the prospective eXtraordinary babies study to identify early risk factors and targets for intervention. *Am. J. Med. Genet. C Semin. Med. Genet.* **184**, 428–443 (2020).
 24. J. Jiang, Y. Jing, G. J. Cost, J.-C. Chiang, H. J. Kolpa, A. M. Cotton, D. M. Carone, B. R. Carone, D. A. Shivak, D. Y. Guschin, J. R. Pearl, E. J. Rebar, M. Byron, P. D. Gregory, C. J. Brown, F. D. Urnov, L. L. Hall, J. B. Lawrence, Translating dosage compensation to trisomy 21. *Nature* **500**, 296–300 (2013).
 25. S. F. Pinter, A tale of two cities: How Xist and its partners localize to and silence the bicompartamental X. *Semin. Cell Dev. Biol.* **56**, 19–34 (2016).
 26. A. Wutz, R. Jaenisch, A shift from reversible to irreversible X inactivation is triggered during ES cell differentiation. *Mol. Cell* **5**, 695–705 (2000).
 27. A. Kohlmaier, F. Savarese, M. Lachner, J. Martens, T. Jenuwein, A. Wutz, A chromosomal memory triggered by Xist regulates histone methylation in X inactivation. *PLoS Biol.* **2**, E171 (2004).
 28. F. Savarese, K. Flahndorfer, R. Jaenisch, M. Busslinger, A. Wutz, Hematopoietic precursor cells transiently reestablish permissiveness for X inactivation. *Mol. Cell Biol.* **26**, 7167–7177 (2006).
 29. R. Agrelo, A. Souabni, M. Novatchkova, C. Haslinger, M. Leeb, V. Komnenovic, H. Kishimoto, L. Gresh, T. Kohwi-Shigematsu, L. Kenner, A. Wutz, SATB1 defines the developmental context for gene silencing by Xist in lymphoma and embryonic cells. *Dev. Cell* **16**, 507–516 (2009).
 30. J. T. Czerwikowski, J. B. Lawrence, Silencing trisomy 21 with XIST in neural stem cells promotes neuronal differentiation. *Dev. Cell* **52**, 294–308.e3 (2020).
 31. S. Guidi, P. Bonasoni, C. Ceccarelli, D. Santini, F. Gualtieri, E. Ciani, R. Bartesaghi, Neurogenesis impairment and increased cell death reduce total neuron number in the hippocampal region of fetuses with Down syndrome. *Brain Pathol.* **18**, 180–197 (2008).
 32. G. Zdaniuk, T. Wierzb-Bobrowicz, G. M. Szpak, T. Stepień, Astroglia disturbances during development of the central nervous system in fetuses with Down's syndrome. *Folia Neuropathol.* **49**, 109–114 (2011).
 33. J. Lu, G. Esposito, C. Scuderì, L. Steardo, L. C. Delli-Bovi, J. L. Hecht, B. C. Dickinson, C. J. Chang, T. Mori, V. Sheen, S100B and APP promote a gliocentric shift and impaired neurogenesis in down syndrome neural progenitors. *PLOS ONE* **6**, e22126 (2011).
 34. J. Lu, G. Lian, H. Zhou, G. Esposito, L. Steardo, L. C. Delli-Bovi, J. L. Hecht, Q. R. Lu, V. Sheen, OLIG2 over-expression impairs proliferation of human Down syndrome neural progenitors. *Hum. Mol. Genet.* **21**, 2330–2340 (2012).
 35. S. Guidi, A. Giacomini, F. Stagni, M. Emili, B. Uguagliati, M. P. Bonasoni, R. Bartesaghi, Abnormal development of the inferior temporal region in fetuses with Down syndrome. *Brain Pathol.* **28**, 986–998 (2018).
 36. D. M. Holtzman, D. Santucci, J. Kilbridge, J. Chua-Couzens, D. J. Fontana, S. E. Daniels, R. M. Johnson, K. Chen, Y. Sun, E. Carlson, E. Allea, C. J. Epstein, W. C. Mobley, Developmental abnormalities and age-related neurodegeneration in a mouse model of Down syndrome. *Proc. Natl. Acad. Sci. U.S.A.* **93**, 13333–13338 (1996).
 37. N. Kurabayashi, M. D. Nguyen, K. Sanada, DYRK1A overexpression enhances STAT activity and astroglialogenesis in a Down syndrome mouse model. *EMBO Rep.* **16**, 1548–1562 (2015).
 38. F. Stagni, A. Giacomini, M. Emili, B. Uguagliati, M. P. Bonasoni, R. Bartesaghi, S. Guidi, Subicular hypotrophy in fetuses with Down syndrome and in the Ts65Dn model of Down syndrome. *Brain Pathol.* **29**, 366–379 (2019).
 39. A. S. Lubiniecki, W. A. Blattner, G. M. Martin, P. J. Fialkow, H. Dosik, C. Eatherly, J. F. Fraumeni, SV40 T-antigen expression in cultured fibroblasts from patients with Down syndrome and their parents. *Am. J. Hum. Genet.* **31**, 469–477 (1979).
 40. L. C. Laurent, I. Ulitsky, I. Slavin, H. Tran, A. Schork, R. Morey, C. Lynch, J. V. Harness, S. Lee, M. J. Barrero, S. Ku, M. Martynova, R. Semechkin, V. Galat, J. Gottesfeld, J. C. I. Belmonte, C. Murry, H. S. Keirstead, H. S. Park, U. Schmidt, A. L. Laslett, F. J. Muller, C. M. Nievergelt, R. Shamir, J. F. Loring, Dynamic changes in the copy number of pluripotency and cell proliferation genes in human ESCs and iPSCs during reprogramming and time in culture. *Cell Stem Cell* **8**, 106–118 (2011).
 41. S. M. Taapken, B. S. Nisler, M. A. Newton, T. L. Sampsel-Barron, K. A. Leonhard, E. M. McIntire, K. D. Montgomery, Karyotypic abnormalities in human induced pluripotent stem cells and embryonic stem cells. *Nat. Biotechnol.* **29**, 313–314 (2011).
 42. P. Papavassiliou, C. Charalsawadi, K. Rafferty, C. Jackson-Cook, Mosaicism for trisomy 21: A review. *Am. J. Med. Genet. A* **167**, 26–39 (2015).
 43. J. P. Weick, D. L. Held, G. F. Bonadurer, M. E. Doers, Y. Liu, C. Maguire, A. Clark, J. A. Knackert, K. Molinaro, M. Musser, L. Yao, Y. Yin, J. Lu, X. Zhang, S.-C. Zhang, A. Bhattacharyya, Deficits in human trisomy 21 iPSCs and neurons. *Proc. Natl. Acad. Sci. U.S.A.* **110**, 9962–9967 (2013).
 44. Y. Hibaoui, I. Grad, A. Letourneau, M. R. Sailani, S. Dahoun, F. A. Santoni, S. Gimelli, M. Guipponi, M. F. F. Pelte, F. Béna, S. E. Antonarakis, A. Feki, Modelling and rescuing

- neurodevelopmental defect of Down syndrome using induced pluripotent stem cells from monozygotic twins discordant for trisomy 21. *EMBO Mol. Med.* **6**, 259–277 (2014).
45. A. Murray, A. Letourneau, C. Canzonetta, E. Stathaki, F. Sloan-Bena, R. Abrehart, P. Goh, S. Lim, C. Baldo, F. Dagna-Bricarelli, S. Hannan, M. Mortensen, D. Ballard, D. Syndercombe Court, N. Fusaki, M. Hasegawa, T. G. Smart, C. Bishop, S. E. Antonarakis, J. Groet, D. Nizetic, Brief report: Isogenic induced pluripotent stem cell lines from an adult with mosaic down syndrome model accelerated neuronal ageing and neurodegeneration. *Stem Cells* **33**, 2077–2084 (2015).
 46. G. A. MacLean, T. F. Menne, G. Guo, D. J. Sanchez, I.-H. Park, G. Q. Daley, S. H. Orkin, Altered hematopoiesis in trisomy 21 as revealed through in vitro differentiation of isogenic human pluripotent cells. *Proc. Natl. Acad. Sci. U.S.A.* **109**, 17567–17572 (2012).
 47. M. Inoue, K. Kajiwara, A. Yamaguchi, T. Kiyono, O. Samura, H. Akutsu, H. Sago, A. Okamoto, A. Umezawa, Autonomous trisomic rescue of Down syndrome cells. *Lab. Invest.* **99**, 885–897 (2019).
 48. G. Csankovszki, B. Panning, B. Bates, J. R. Pehrson, R. Jaenisch, Conditional deletion of Xist disrupts histone macroH2A localization but not maintenance of X inactivation. *Nat. Genet.* **22**, 323–324 (1999).
 49. G. Csankovszki, A. Nagy, R. Jaenisch, Synergism of Xist RNA, DNA methylation, and histone hypoacetylation in maintaining x chromosome inactivation. *J. Cell Biol.* **153**, 773–784 (2001).
 50. N. Moullan, L. Mouchiroud, X. Wang, D. Ryu, E. G. Williams, A. Mottis, V. Jovaisaite, M. V. Frochoux, P. M. Quiros, B. Deplancke, R. H. Houtkooper, J. Auwerx, Tetracyclines disturb mitochondrial function across eukaryotic models: A call for caution in biomedical research. *Cell Rep.* **10**, 1681–1691 (2015).
 51. A. Izzo, N. Mollo, M. Nitti, S. Paladino, G. Cali, R. Genesio, F. Bonfiglio, R. Cicatiello, M. Barbato, V. Sarnataro, A. Conti, L. Nitsch, Mitochondrial dysfunction in Down syndrome: Molecular mechanisms and therapeutic targets. *Mol. Med.* **24**, 2 (2018).
 52. D. Valenti, N. Braidy, D. De Rasmo, A. Signorile, L. Rossi, A. G. Atanasov, M. Volpicella, A. Henrion-Caude, S. M. Nabavi, R. A. Vacca, Mitochondria as pharmacological targets in Down syndrome. *Free Radic. Biol. Med.* **114**, 69–83 (2018).
 53. V. Parra, F. Altamirano, C. P. Hernández-Fuentes, D. Tong, V. Kyrychenko, D. Rotter, Z. Pedrozo, J. A. Hill, V. Eisner, S. Lavandero, J. W. Schneider, B. A. Rothermel, Down syndrome critical region 1 gene, *Rcan1*, helps maintain a more fused mitochondrial network. *Circ. Res.* **122**, e20–e33 (2018).
 54. E. J. Wolvetang, O. M. Bradfield, T. Hatzistavrou, P. J. Crack, J. Busciglio, I. Kola, P. J. Hertzog, Overexpression of the chromosome 21 transcription factor Ets2 induces neuronal apoptosis. *Neurobiol. Dis.* **14**, 349–356 (2003).
 55. C. Noll, A. Tilili, C. Ripoll, L. Mallet, J. L. Paul, J. M. Delabar, N. Janel, Dyrk1a activates antioxidant NQO1 expression through an ERK1/2-Nrf2 dependent mechanism. *Mol. Genet. Metab.* **105**, 484–488 (2012).
 56. Y. Liu, C. Borel, L. Li, T. Müller, E. G. Williams, P. L. Germain, M. Buljan, T. Sajic, P. J. Boersma, W. Shao, M. Faini, G. Testa, A. Beyer, S. E. Antonarakis, R. Aebersold, Systematic proteome and proteostasis profiling in human trisomy 21 fibroblast cells. *Nat. Commun.* **8**, 1212 (2017).
 57. E. Banda, A. McKinsey, N. Germain, J. Carter, N. C. Anderson, L. Gabel, Cell polarity and neurogenesis in embryonic stem cell-derived neural rosettes. *Stem Cells Dev.* **24**, 1022–1033 (2015).
 58. J. W. Linsley, K. Shah, N. Castello, M. Chan, D. Haddad, Z. Doric, S. Wang, W. Leks, J. Mancini, V. Oza, A. Javaherian, K. Nakamura, D. Kokel, S. Finkbeiner, Genetically encoded cell-death indicators (GEDi) to detect an early irreversible commitment to neurodegeneration. *Nat. Commun.* **12**, 5284 (2021).
 59. Y. H. Chang, J. Linsley, J. Lamstein, J. Kalra, I. Epstein, M. Barch, K. Daily, P. Synder, L. Omberg, L. Heiser, S. Finkbeiner, Single cell tracking based on Voronoi partition via stable matching, in *2020 59th IEEE Conference on Decision and Control (CDC)* (IEEE, 2020), pp. 5086–5091.
 60. Y. Giffin-Rao, J. Sheng, B. Strand, K. Xu, L. Huang, M. Medo, K. A. Risgaard, S. Dantinne, S. Mohan, A. Keshan, R. A. Daley, B. Levesque, L. Amundson, R. Reese, A. M. M. Sousa, Y. Tao, D. Wang, S. C. Zhang, A. Bhattacharyya, Altered patterning of trisomy 21 interneuron progenitors. *Stem Cell Rep.* **17**, 1366–1379 (2022).
 61. J. Busciglio, B. A. Yankner, Apoptosis and increased generation of reactive oxygen species in Down's syndrome neurons in vitro. *Nature* **378**, 776–779 (1995).
 62. J. A. Briggs, J. Sun, J. Shepherd, D. A. Ovchinnikov, T. L. Chung, S. P. Nayler, L. P. Kao, C. A. Morrow, N. Y. Thakar, S. Y. Soo, T. Peura, S. Grimmond, E. J. Wolvetang, Integration-free induced pluripotent stem cells model genetic and neural developmental features of Down syndrome etiology. *Stem Cells* **31**, 467–478 (2013).
 63. Y. Shi, P. Kirwan, J. Smith, H. P. C. Robinson, F. J. Livesey, Human cerebral cortex development from pluripotent stem cells to functional excitatory synapses. *Nat. Neurosci.* **15**, 477–486 (2012).
 64. A. M. Maroof, S. Keros, J. A. Tyson, S.-W. Ying, Y. M. Ganat, F. T. Merkle, B. Liu, A. Goulburn, E. G. Stanley, A. G. Elefanty, H. R. Widmer, K. Eggan, P. A. Goldstein, S. A. Anderson, L. Studer, Directed differentiation and functional maturation of cortical interneurons from human embryonic stem cells. *Cell Stem Cell* **12**, 559–572 (2013).
 65. F. Yuan, K. H. Fang, S. Y. Cao, Z. Y. Qu, Q. Li, R. Krencik, M. Xu, A. Bhattacharyya, Y. W. Su, D. Y. Zhu, Y. Liu, Efficient generation of region-specific forebrain neurons from human pluripotent stem cells under highly defined condition. *Sci. Rep.* **5**, 18550 (2015).
 66. A. V. Molofsky, R. Krencik, E. M. Ullian, H.-H. Tsai, B. Deneen, W. D. Richardson, B. A. Barres, D. H. Rowitch, Astrocytes and disease: A neurodevelopmental perspective. *Genes Dev.* **26**, 891–907 (2012).
 67. E. E. Burke, J. G. Chenoweth, J. H. Shin, L. Collado-Torres, S.-K. Kim, N. Micali, Y. Wang, C. Colantuoni, R. E. Straub, D. J. Hoepfner, H.-Y. Chen, A. Sellers, K. Shiban, G. R. Hamersky, M. Diaz Bustamante, B. N. Phan, W. S. Ulrich, C. Valencia, A. Jaishankar, A. J. Price, A. Rajpurohit, S. A. Semick, R. W. Bürl, J. C. Barrow, D. J. Hiler, S. C. Page, K. Martinowich, T. M. Hyde, J. E. Kleinman, K. F. Berman, J. A. Apud, A. J. Cross, N. J. Brandon, D. R. Weinberger, B. J. Maher, R. D. G. McKay, A. E. Jaffe, Dissecting transcriptomic signatures of neuronal differentiation and maturation using iPSCs. *Nat. Commun.* **11**, 462 (2020).
 68. A. Ianevski, A. K. Giri, T. Aittokallio, Fully-automated and ultra-fast cell-type identification using specific marker combinations from single-cell transcriptomic data. *Nat. Commun.* **13**, 1246 (2022).
 69. G. Stamoulis, M. Garieri, P. Makrythanasis, A. Letourneau, M. Guipponi, N. Panousis, F. Sloan-Béna, E. Falconnet, P. Ribaux, C. Borel, F. Santoni, S. E. Antonarakis, Single cell transcriptome in aneuploidies reveals mechanisms of gene dosage imbalance. *Nat. Commun.* **10**, 4495 (2019).
 70. S. Hunter, J. Hendrix, J. Freeman, R. D. Dowell, M. A. Allen, Transcription dosage compensation does not occur in Down syndrome. *BMC Biol.* **21**, 228 (2023).
 71. C. Hafemeister, R. Satija, Normalization and variance stabilization of single-cell RNA-seq data using regularized negative binomial regression. *Genome Biol.* **20**, 296 (2019).
 72. R. Tobe, S. Naranjo-Suarez, R. A. Everley, B. A. Carlson, A. A. Turanov, P. A. Tsuji, M.-H. Yoo, S. P. Gygi, V. N. Gladyshev, D. L. Hatfield, High error rates in selenocysteine insertion in mammalian cells treated with the antibiotic doxycycline, chloramphenicol, or geneticin. *J. Biol. Chem.* **288**, 14709–14715 (2013).
 73. I. de Toma, C. Sierra, M. Dierssen, Meta-analysis of transcriptomic data reveals clusters of consistently deregulated gene and disease ontologies in Down syndrome. *PLOS Comput. Biol.* **17**, e1009317 (2021).
 74. R. Beckervordersandforth, Mitochondrial metabolism-mediated regulation of adult neurogenesis. *Brain Plast.* **3**, 73–87 (2017).
 75. K. Kawatani, T. Nambara, N. Nawa, H. Yoshimatsu, H. Kusakabe, K. Hirata, A. Tanave, K. Sumiyama, K. Banno, H. Taniguchi, H. Arahori, K. Ozono, Y. Kitabatake, A human isogenic iPSC-derived cell line panel identifies major regulators of aberrant astrocyte proliferation in Down syndrome. *Commun. Biol.* **4**, 730 (2021).
 76. F. Neri, S. Rapelli, A. Krepelova, D. Incarnato, C. Parlato, G. Basile, M. Maldotti, F. Anselmi, S. Oliviero, Intragenic DNA methylation prevents spurious transcription initiation. *Nature* **543**, 72–77 (2017).
 77. G. O. Mizuno, Y. Wang, G. Shi, Y. Wang, J. Sun, S. Papadopoulos, G. J. Broussard, E. K. Unger, W. Deng, J. Weick, A. Bhattacharyya, C.-Y. Chen, G. Yu, L. L. Looger, L. Tian, Aberrant calcium signaling in astrocytes inhibits neuronal excitability in a human Down syndrome stem cell model. *Cell Rep.* **24**, 355–365 (2018).
 78. Á. Fernández-blanco, M. Dierssen, Rethinking intellectual disability from neuro- to astro-pathology. *int. J. Mol. Sci.* **21**, 9039 (2020).
 79. J. Wang, C. M. Syrett, M. C. Kramer, A. Basu, M. L. Atchison, M. C. Anguera, Unusual maintenance of X chromosome inactivation predisposes female lymphocytes for increased expression from the inactive X. *Proc. Natl. Acad. Sci. U.S.A.* **113**, E2029–E2038 (2016).
 80. J. C. Chiang, J. Jiang, P. E. Newburger, J. B. Lawrence, Trisomy silencing by XIST normalizes Down syndrome cell pathogenesis demonstrated for hematopoietic defects in vitro. *Nat. Commun.* **9**, 5180 (2018).
 81. D. Rocks, M. Shukla, L. Ouldibbat, S. C. Finemann, A. Kalluchi, M. J. Rowley, M. Kundakovic, Sex-specific multi-level 3D genome dynamics in the mouse brain. *Nat. Commun.* **13**, 3438 (2022).
 82. J. C. Chow, L. L. Hall, S. E. L. Baldry, N. P. Thorogood, J. B. Lawrence, C. J. Brown, Inducible XIST-dependent X-chromosome inactivation in human somatic cells is reversible. *Proc. Natl. Acad. Sci. U.S.A.* **104**, 10104–10109 (2007).
 83. A. D. Kelsey, C. Yang, D. Leung, J. Minks, T. Dixon-McDougall, S. E. L. Baldry, A. B. Bogutz, L. Lefebvre, C. J. Brown, Impact of flanking chromosomal sequences on localization and silencing by the human non-coding RNA XIST. *Genome Biol.* **16**, 208 (2015).
 84. A. Loda, J. H. Brandsma, I. Vassilev, N. Servant, F. Loos, A. Amirnasr, E. Splinter, E. Barillot, R. A. Poot, E. Heard, J. Gribnau, Genetic and epigenetic features direct differential efficiency of Xist-mediated silencing at X-chromosomal and autosomal locations. *Nat. Commun.* **8**, 690 (2017).
 85. A. Wutz, Epigenetic alterations in human pluripotent stem cells: A tale of two cultures. *Cell Stem Cell* **11**, 9–15 (2012).
 86. P. Bansal, D. T. Ahern, Y. Kondaveeti, C. W. Qiu, S. F. Pinter, Contiguous erosion of the inactive X in human pluripotency concludes with global DNA hypomethylation. *Cell Rep.* **35**, 109215 (2021).

87. C. Lois, E. J. Hong, S. Pease, E. J. Brown, D. Baltimore, Germline transmission and tissue-specific expression of transgenes delivered by lentiviral vectors. *Science* **295**, 868–872 (2002).
88. R. C. DeKaveler, V. M. Choi, E. A. Moehle, D. E. Paschon, D. Hockemeyer, S. H. Meijnsing, Y. Sancak, X. Cui, E. J. Steine, J. C. Miller, P. Tam, V. V. Bartsevich, X. Meng, I. Rupniewski, S. M. Gopalan, H. C. Sun, K. J. Pitz, J. M. Rock, L. Zhang, G. D. Davis, E. J. Rebar, I. M. Cheeseman, K. R. Yamamoto, D. M. Sabatini, R. Jaenisch, P. D. Gregory, F. D. Urnov, Functional genomics, proteomics, and regulatory DNA analysis in isogenic settings using zinc finger nuclease-driven transgenesis into a safe harbor locus in the human genome. *Genome Res.* **20**, 1133–1142 (2010).
89. P. Liu, N. A. Jenkins, N. G. Copeland, A highly efficient recombineering-based method for generating conditional knockout mutations. *Genome Res.* **13**, 476–484 (2003).
90. S. X. Chen, A. B. Osipovich, A. Ustione, L. A. Potter, S. Hipkens, R. Gangula, W. Yuan, D. W. Piston, M. A. Magnuson, Quantification of factors influencing fluorescent protein expression using RMCE to generate an allelic series in the ROSA26 locus in mice. *Dis. Model. Mech.* **4**, 537–547 (2011).
91. Z. Zhu, F. González, D. Huangfu, The iCRISPR platform for rapid genome editing in human pluripotent stem cells. *Methods Enzymol.* **546**, 215–250 (2014).
92. F. González, Z. Zhu, Z.-D. Shi, K. Lelli, N. Verma, Q. V. Li, D. Huangfu, An iCRISPR platform for rapid, multiplexable, and inducible genome editing in human pluripotent stem cells. *Cell Stem Cell* **15**, 215–226 (2014).
93. F. A. Ran, P. P. D. Hsu, J. Wright, V. Agarwala, D. A. Scott, F. Zhang, Genome engineering using the CRISPR-Cas9 system. *Nat. Protoc.* **8**, 2281–2308 (2013).
94. C. R. Nicholas, J. Chen, Y. Tang, D. G. Southwell, N. Chalmers, D. Vogt, C. M. Arnold, Y. J. J. Chen, E. G. Stanley, A. G. Elefanty, Y. Sasaki, A. Alvarez-Buylla, J. L. R. Rubenstein, A. R. Kriegstein, Functional maturation of hPSC-derived forebrain interneurons requires an extended timeline and mimics human neural development. *Cell Stem Cell* **12**, 573–586 (2013).
95. M. Arrasate, S. Mitra, E. S. Schweitzer, M. R. Segal, S. Finkbeiner, Inclusion body formation reduces levels of mutant huntingtin and the risk of neuronal death. *Nature* **431**, 805–810 (2004).
96. C. McQuin, A. Goodman, V. Chernyshev, L. Kamentsky, A. Cimini, K. W. Karhohs, M. Doan, L. Ding, S. M. Rafelski, D. Thirstrup, W. Wiegraebe, S. Singh, T. Becker, J. C. Caicedo, A. E. Carpenter, CellProfiler 3.0: Next-generation image processing for biology. *PLOS Biol.* **16**, e2005970 (2018).
97. B. Bushnell, BBTools; sourceforge.net/projects/bbmap/.
98. R. Patro, G. Duggal, M. I. Love, R. A. Irizarry, C. Kingsford, Salmon provides fast and bias-aware quantification of transcript expression. *Nat. Methods* **14**, 417–419 (2017).
99. M. I. Love, W. Huber, S. Anders, V. Tusher, E. Banks, T. Fennell, A. O'Donnell-Luria, J. Ware, A. Hill, B. Cummings, Moderated estimation of fold change and dispersion for RNA-seq data with DESeq2. *Genome Biol.* **15**, 550 (2014).
100. T. Wu, E. Hu, S. Xu, M. Chen, P. Guo, Z. Dai, T. Feng, L. Zhou, W. Tang, L. Zhan, X. Fu, S. Liu, X. Bo, G. Yu, clusterProfiler 4.0: A universal enrichment tool for interpreting omics data. *Innovation* **2**, 100141 (2021).
101. M. J. Aryee, A. E. Jaffe, H. Corrada-Bravo, C. Ladd-Acosta, A. P. Feinberg, K. D. Hansen, R. A. Irizarry, Minfi: A flexible and comprehensive Bioconductor package for the analysis of Infinium DNA methylation microarrays. *Bioinformatics* **30**, 1363–1369 (2014).
102. D. Kim, J. M. Paggi, C. Park, C. Bennett, S. L. Salzberg, Graph-based genome alignment and genotyping with HISAT2 and HISAT-genotype. *Nat. Biotechnol.* **37**, 907–915 (2019).
103. S. E. Castel, P. Mohammadi, W. K. Chung, Y. Shen, T. Lappalainen, Rare variant phasing and haplotypic expression from RNA sequencing with phASER. *Nat. Commun.* **7**, 12817 (2016).
104. Y. Hao, S. Hao, E. Andersen-Nissen, W. M. Mauck, S. Zheng, A. Butler, M. J. Lee, A. J. Wilk, C. Darby, M. Zager, P. Hoffman, M. Stoeckius, E. Papalexi, E. P. Mimitou, J. Jain, A. Srivastava, T. Stuart, L. M. Fleming, B. Yeung, A. J. Rogers, J. M. McElrath, C. A. Blish, R. Gottardo, P. Smibert, R. Satija, Integrated analysis of multimodal single-cell data. *Cell* **184**, 3573–3587.e29 (2021).

Acknowledgments: We are grateful to G. Carmichael and J. Li for comments on our manuscript. We also thank the University of Connecticut's Cell and Genome Engineering Core and Center for Genome Innovation for reprogramming, as well as mRNA-seq, CytoSNP, linked-read WGS, and methylEPIC core services, respectively. **Funding:** This work was supported by grants from the LuMind IDSC Foundation and the NIH (R35GM124926, with additional support from R01HL141324) to S.F.P. Support for work conducted at the Gladstone Institutes (to S.F.) came from R01 AG064579 with additional support from R01 LM013617, RF1 NS128800, and the JSRM Foundation. Work at the Centre for Genomic Regulation (to M.D.) was supported by the Fondation Jérôme Lejeune #2002, Fundació La Marató De TV 3 202212-30-31-32, and Agencia Estatal de Investigación (PID2019-110755RB-I00/AEI/10.13039/501100011033). We acknowledge support of the Spanish Ministry of Science and Innovation to the EMBL partnership, the Centro de Excelencia Severo Ochoa and the CERCA Programme/Generalitat de Catalunya, and FPU fellowship (FPU19/04789) from Ministerio de Universidades (to M.S.-N.) The CIBER of Rare Diseases is an initiative of the ISCIII. **Author contributions:** Conceptualization: P.B., E.C.B., and S.F.P. Methodology: P.B., E.C.B., H.R.G.-D., C.E.S., J.W.L., M.S.-N., and S.F.P. Investigation: P.B., E.C.B., H.R.G.-D., J.W.L., N.A., D.T.A., Y.K., R.E.M., M.N., C.D., M.S.-N., and S.W. Project administration: S.F.P. Writing—original draft: P.B., E.C.B., and S.F.P. Writing—review and editing: S.F., M.D., and S.F.P. **Competing interests:** J.W.L. is a founder of Operant BioPharma. His work in this study was conducted as an employee and scientific consultant of Gladstone Institutes. The other authors declare that they have no competing interests. **Data and materials availability:** All data needed to evaluate the conclusions in the paper are present in the paper and/or the Supplementary Materials. Unique reagents generated in this study can be provided with applicable processing and shipping fees through the University of Connecticut Cell and Genome Engineering Core, pending scientific review and a completed material transfer agreement. Requests should be submitted to S.F.P. CytoSNP-850k and methylEPIC array, as well as linked-read WGS, bulk mRNA-seq and single-nucleus RNA-seq data, are deposited under study accession no. phs002397.v1.p1 in the database of Genotypes and Phenotypes (dbGaP). Analysis code is available from <https://github.uconn.edu/sfp-lab/T21-XIST> and as a Dryad dataset under <https://doi.org/10.5061/dryad.8kpr4xvc>.

Submitted 23 August 2023

Accepted 3 May 2024

Published 7 June 2024

10.1126/sciadv.adj0385